Responses of Model Cortical Neurons to Temporal Interference Stimulation and Related Transcranial Alternating Current Stimulation Modalities

Boshuo Wang[1], Aman S. Aberra[2,#], Warren M. Grill[2,3,4,5], Angel V. Peterchev[1,2,3,5,*]

[1] Department of Psychiatry and Behavioral Sciences, School of Medicine, Duke University, Durham, NC 27710, USA

[2] Department of Biomedical Engineering, School of Engineering, Duke University, Durham, NC 27708, USA

[3] Department of Electrical and Computer Engineering, School of Engineering, Duke University, Durham, NC 27708, USA

[4] Department of Neurobiology, School of Medicine, Duke University, Durham, NC 27710, USA

[5] Department of Neurosurgery, School of Medicine, Duke University, Durham, NC 27710, USA

[*] Corresponding author: angel.peterchev@duke.edu

[#] A. S. Aberra is currently with the Department of Biological Sciences, Dartmouth College, Hanover, NH 03755, USA.

Keywords: temporal interference stimulation, transcranial alternating current stimulation, kilohertz stimulation, computational simulation, neuron model

Abstract

Objective. Temporal interference stimulation (TIS) was proposed as a non-invasive, focal, and steerable deep brain stimulation method. However, the mechanisms underlying experimentally-observed suprathreshold TIS effects are unknown, and prior simulation studies had limitations in the representations of the TIS electric field (E-field) and cerebral neurons. We examined the E-field and neural response characteristics for TIS and related transcranial alternating current stimulation modalities.

Approach. We simulated a range of stimulation parameters in cortical neurons, including different orientations, frequencies, amplitude ratios, amplitude modulation, and phase difference of the E-fields, and obtained thresholds for both activation and conduction block.

Main results. Where the two E-fields had similar amplitudes, typically at the target region, TIS generated an amplitude-modulated total E-field. Due to the phase difference of the individual E-fields, the total TIS E-field vector also exhibited rotation where the orientations of the two E-fields were not aligned, which generally occurs at the target region. TIS activation thresholds (75–230 V/m) were similar to high-frequency stimulation with or without

modulation and/or rotation. Outside the target region, the TIS E-field was dominated by the high-frequency carrier, with minimal amplitude modulation and/or rotation, and it was less effective at activation and more effective at block. Unlike amplitude-modulated high-frequency stimulation, TIS generated conduction block with some orientations and amplitude ratios of individual E-field at very high amplitudes of the total E-field (>1700 V/m).

Significance. The complex 3D properties of the TIS E-fields should be accounted for in computational and experimental studies. The mechanisms of suprathreshold cortical TIS appear to involve neural activity block and periodic activation or onset response, consistent with computational studies of peripheral axons. These phenomena occur at E-field strengths too high to be delivered tolerably through scalp electrodes and may inhibit endogenous activity in off-target regions, suggesting limited significance of suprathreshold TIS.

1 Introduction

Transcranial electric or magnetic stimulation can modulate the activity of neurons in the brain non-invasively to treat neurological and psychiatric disorders [1–6]. Compared to invasive methods, the electric field (E-field) distribution of transcranial stimulation is more diffuse and shallower due to the large distance between the stimulation sources and the brain and the high conductivity contrast of the tissue layers [7]. For transcranial electrical stimulation (TES), the typical cortical area activated or exposed to significant E-field strength (e.g., more than half the maximum E-field) is on the order of square centimeters [8,9]. For magnetic stimulation (TMS), the fundamental depth-focality trade-off shows that activation of deep targets would result in widespread activation of more superficial brain regions [10,11]. Efforts to improve the spatial characteristics such as focality and depths of conventional stimulation methods mostly rely on improved geometric design of the stimulation devices including electrode montages [12–15] and coil designs [11].

Methods that use the temporal domain and intrinsic neuronal properties were proposed as a means to achieve more focal and/or deep transcranial electrical [16,17] or magnetic [18] stimulation. These methods use multiple stimulation channels, e.g., comprised of separate pairs of scalp electrodes, to generate individual E-fields in the head with different temporal waveforms. Temporal interference stimulation (TIS), also referred to as interferential current therapy and applied as a neuromuscular treatment between the 1960s and 1990s [19,20], was proposed for non-invasive brain stimulation [16]. In TIS, two high frequency (> 1 kHz) sinusoidal E-fields are applied with a slight frequency difference to create an amplitude-modulated (AM) total E-field through temporal interference. Borrowing terminology from radio technology, neurons are hypothesized to demodulate the low frequency (< 100 Hz) amplitude envelope of the summed E-field waveform via transmembrane current rectification due to the nonlinear properties of ion channels. Under this assumption, activation would occur mostly in deeper brain regions where the E-field amplitudes of the stimulation channels are similar and therefore the modulation depth (i.e., extent of amplitude change due to the modulation) of the total E-field waveform is large. On the other hand, superficial brain areas would be unaffected, as the mismatch in E-field amplitudes generates a negligible low frequency envelope, and neurons are thought to be insensitive to the large amplitude kHz carrier wave. Without repositioning

the electrodes, TIS could steer the site of stimulation by adjusting the relative amplitudes of each channel to shift the region where the E-fields generate the largest amplitude and/or modulation depth of interference [16].

Grossman et al. [16] reported experimental neuronal responses to TIS in the anesthetized mouse brain with current amplitude 2–5 times higher than the threshold for low frequency transcranial alternating current stimulation (tACS), whereas high frequency (kHz) tACS could not evoke responses even at seven times higher current amplitudes. However, the mechanism underlying these effects and the potential application to transcranial stimulation in humans remains unclear. One interpretation is that unmodulated kHz tACS does not significantly affect neurons, putatively due to low-pass filtering at the neuronal membrane, whereas the amplitude modulation exhibited by the summed TIS E-field generates low frequency transmembrane potentials that periodically activate the neurons. This explanation, however, does not take into account the fact that kHz stimulation can result in transient or sustained firing and, at higher amplitudes, neuronal activity block [21–24]. These responses to kHz stimulation cannot be ignored given that the unmodulated kHz E-field has stronger absolute amplitude than the low frequency modulation envelope, and that the neuronal membrane can respond to kHz stimuli since time constants of the cortical response to transcranial stimulation are around 150–250 μs [25–27]. Moreover, because the neuronal membrane should low-pass filter modulated and unmodulated kHz waveforms to a similar degree, membrane filtering does not favor the modulated E-field [23,28]. Even if the effects of the unmodulated kHz stimulus were not detected with specific measurements, this does not necessarily mean that neurons were not significantly impacted. It is possible, for example, that kHz neuronal block suppress neural responses in regions away from the target [23]. Focality of activation can be achieved in such scenarios, but at the cost of affecting endogenous brain activity in non-target regions.

Several studies explored the mechanisms of TIS, but had limitations in their methods and were not designed to distinguish between the competing mechanistic explanations outlined above. For example, the Grossman et al. [16] study was in anesthetized mice, and while TIS did not appear to activate off-target brain regions, it is unclear whether it blocked or disrupted endogenous brain activity outside the target. Computational studies of suprathreshold TIS focused on activation of isolated axons (fibers of passage) [23,29,30], which do not fully capture effects on cortical neurons. The combination of the two TIS current waveforms results in a three-dimensional (3D)

time-varying E-field that can interact in complex ways with 3D cortical neurons [31], but the TIS E-fields and their effect on neurons were analyzed in one dimension (1D), either along the direction of largest modulation depth or in a predetermined direction such as the radial direction of the gray matter or along fiber bundles in the white matter [15,16,23,29,30,32–36]. Some studies explored the modulation of ongoing cortical activity using TIS in the regime of subthreshold field strength of conventional tACS [30,32]; however, they did not provide mechanistic information relevant to deep brain activation by TIS.

Translation of TIS from animal studies to clinical applications poses further challenges. With the same current amplitude, E-fields generated in the human brain are two orders-of-magnitude smaller than those in mice due to differences in head size and cortical geometry. Conventional tACS currents delivered via scalp electrodes are limited to a few milliamps to be tolerable without anesthesia, generating subthreshold E-fields on the order of only 0.1 to 1 $\mathrm{V/m}$ throughout the human brain [15,35,37,38]. Suprathreshold TIS in humans would therefore require much higher current amplitudes. Hence, estimation of TIS E-field thresholds would provide key information for determining the clinical applicability of TIS.

To understand the biophysics underlying TIS for suprathreshold deep brain stimulation, we analyzed the spatiotemporal characteristics of the TIS E-field and simulated the response of individual cortical neurons to TIS and several related tACS modalities. The TIS E-field exhibited some unique properties that potentially impacts neural activation and are not reproduced with AM-tACS. The simulations show that conduction block of ongoing off-target activity can occur and the mechanisms that can account for the periodic neural activation by TIS require field strengths that are not feasible in humans due to the high currents that need to be applied to the scalp.

2 Methods

2.1 Characteristics of TIS E-field

Unlike conventional tACS, the E-field of TIS consists of two or more spatial components that have different temporal characteristic. Whereas the E-field of each channel is considered quasi-static, and thus separable into spatial and temporal components [39,40], the total TIS E-field is not. Each channels' E-field can be described as $\boldsymbol{E}_n = \boldsymbol{S}_n(\boldsymbol{s}) \cdot T_n(t)$, where $\boldsymbol{s}$ is the macroscopic spatial coordinate vector within the brain, t is time, and $n = 1, 2, \ldots$

is the channel number. For simplicity, only two-channel TIS is considered and the temporal functions of the tACS channels are normalized: $T_n(t) = \sin(\omega_n t + \alpha_n)$, where ω_n and α_n are their frequency and initial phase. The E-field amplitudes are given according to their spatial distributions $|\boldsymbol{S}_n|$. Specifically for transcranial stimulation, the uniform E-field approximation on the microscopic scale of individual neurons [41] is considered so that $\boldsymbol{S}_n$ is constant for individual neurons but varies depending on cortical location [42].

2.1.1 Aligned E-fields

With $\omega_1 \neq \omega_2$, a 1D AM interferential waveform exists only where the two local E-fields are aligned or anti-aligned (Figure 1A$_i$):

$$|\boldsymbol{E}_{\mathrm{TIS}}| = A_{\mathrm{TIS}}(t) \cdot \sin\big(\alpha_{\mathrm{TIS}}(t)\big) \quad .$$

where A_{TIS} and α_{TIS} are the envelope and instantaneous phase of the oscillation. The envelope

$$A_{\mathrm{TIS}}(t) = \sqrt{A_1^2 + A_2^2 + 2A_1A_2\cos(\Delta\omega t + \Delta\alpha)}$$

has frequency $\Delta\omega = \omega_2 - \omega_1$ and maximum and minimum amplitudes of $A_1 + A_2$ and $|A_1 - A_2|$, in which the individual field amplitudes are $A_1 = |\boldsymbol{S}_1|$ and $A_2 = |\boldsymbol{S}_2|$, and the initial phase difference $\Delta\alpha = \alpha_2 - \alpha_1$ is 0° or 180° for TIS (aligned and anti-aligned, respectively). The instantaneous phase is

$$\alpha_{\mathrm{TIS}}(t) = \omega_1 t + \alpha_1 + \arctan\frac{A_2\sin(\Delta\omega t + \Delta\alpha)}{A_1 + A_2\cos(\Delta\omega t + \Delta\alpha)} \quad .$$

The TIS waveform's carrier frequency

$$\omega_{\mathrm{TIS}}(t) = \frac{\mathrm{d}\alpha_{\mathrm{TIS}}}{\mathrm{d}t} = \frac{A_1^2\omega_1 + A_2^2\omega_2 + A_1A_2(\omega_1 + \omega_2)\cos(\Delta\omega t + \Delta\alpha)}{A_1^2 + A_2^2 + 2A_1A_2\cos(\Delta\omega t + \Delta\alpha)}$$

is constant and equals the mean of the two high frequencies only for equal amplitudes. For $A_1 \neq A_2$, however, ω_{TIS} has low frequency jitter around the frequency of the channel with the larger amplitude (Figure 1A$_{ii}$):

$$\bar{\omega}_{\mathrm{TIS}} = \frac{\omega_1 + \omega_2}{2} + \frac{\Delta\omega}{2}\mathrm{sgn}(A_2 - A_1) = \begin{cases} \omega_1 & A_1 > A_2 \\ \dfrac{\omega_1 + \omega_2}{2} & A_1 = A_2 \\ \omega_2 & A_1 < A_2 \end{cases} \quad .$$

Thus, TIS differs from AM-tACS, which has a constant carrier frequency.

The peak of the low frequency envelope can be out of phase by 180° and the high frequency oscillations have different phase shifts throughout their common low frequency period at different cortical locations, depending on the alignment of the E-fields and their amplitude ratio (Figure $1A_i$). This is similar to the traveling wave observed for two-channel tACS with the same frequency but a non-zero phase difference [43].

2.1.2 Non-aligned E-fields

For non-aligned E-fields, the total E-field must be considered in 3D, and not just along the direction of maximum modulation (Figure $1B_i$). In the plane spanned by the two E-field vectors, the total E-field traces out a Lissajous curve bounded by a parallelogram determined by the amplitude, orientation, and phase of the two E-fields (Figure $1B_{ii}$). For E-fields with similar amplitudes and a large angle (e.g., between 60° and 120°) between them, the total E-field alternates between oscillations and rotations at low frequency. The oscillation and rotation correspond to periods in time when the two E-fields are in-phase and out-of-phase and can be characterized by the ratio of the minimum and maximum E-field amplitude during one high frequency cycle.

Unlike any 1D E-field projections that do not contain low-frequency content [23], the amplitude of the rotating E-field does contain low-frequency power (Figure $1B_{iii}$ and $1B_{iv}$) and field rotation could be contributing to stimulation by TIS. For example, multi-electrode tACS with phase-shift generates global traveling waves and local rotation for the E-field [43], and rotational field TMS, applied using two perpendicular figure-of-eight coils driven with the same current waveforms with a 90° phase shift, exhibited lower thresholds and stronger evoked responses [44–46]. The rotational E-field is hypothesized to sweep across the neural population and simultaneously activate neurons with different directional sensitivity [44,46].

Given the large difference between the volumes of brain where the two TIS E-fields are (approximately) aligned versus not aligned, 1D parameters such as modulation depth, carrier frequency, and envelope do not encompass the full spectrum of TIS scenarios. Capturing the spatial variations in E-field dynamics within individual neurons in computational simulations requires neuronal models with realistic morphology instead of point neuron models. For a given amplitude ratio of the stimulation channels, only the ratio of the E-field amplitude can be specified for any neuron under the quasi-uniform approximation, and no single modulation depth can be defined because the waveform of the E-fields projected along the neural cables varies for different neuronal compartments.

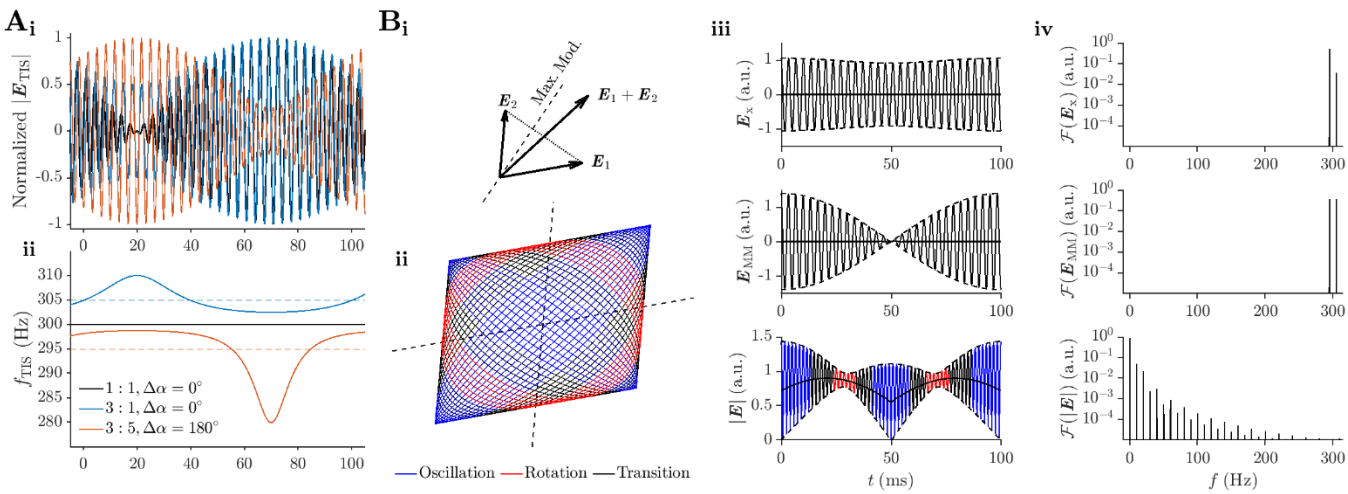

Figure 1. Time and frequency domain characteristics of TIS E-fields

A. Characteristic of the total TIS E-field of two aligned (blue and black) or anti-aligned (orange) E-fields with various amplitude ratios. The channels have relatively low frequencies (295 Hz and 305 Hz) for better visualization. **i.** For aligned E-fields (blue and black), the high frequency oscillations of the total E-fields (normalized) are in-phase only at the peaks of their envelopes and shift out of phase at the troughs. For anti-aligned fields (orange), the envelopes themselves are 180° out-of-phase compared to the those of aligned E-fields (blue or black), whereas the carrier could be in-phase at a peak/trough (orange and blue, in-phase at $t \approx 120$ ms) or in between peak and trough (red and black, in-phase at $t \approx 40$ ms). Such phase differences can result in asynchronous neural activation across different cortical locations. **ii.** The carrier frequency of the total TIS E-field includes low frequency jitter around the frequency of the E-field with larger amplitude, unlike constant-frequency AM-tACS. **B.** Characteristics of two non-aligned E-fields with an amplitude ratio of 5:4 and a 75° angle. **i.** Considering the E-fields in 3D reveals field rotation previously not considered. The two E-fields of TIS span a plane containing the direction of maximum modulation (Max. Mod., dashed line), which most studies use for analysis of stimulation characteristics, such as amplitude of envelope and modulation depth. **ii.** The end point of the total E-field vector traces out a Lissajous curve, which alternates between oscillatory (blue) and rotational (red) periods. Here, oscillation and rotation are (arbitrarily) defined as the E-field magnitude having a ratio of minimum versus maximum smaller than 1/3 or larger than 2/3 during one high frequency cycle, respectively. **iii.** The total E-field projected along any direction, for example the x-axis ($\boldsymbol{E}_x$, top row) or the direction of maximum modulation ($\boldsymbol{E}_{\mathrm{MM}}$, middle row), has a low frequency

envelope (dashed lines). The oscillations, however, average out to zero (thick line) and therefore the waveform does not contain low frequency energy. In contrast, the E-field magnitude (bottom row) has low frequency content that could be a driving factor of TIS. **iv.** The corresponding spectrum of the E-fields in iii. $\mathcal{F}$: Fourier transform. a.u.: arbitrary units.

2.2 Neuronal response to TIS and other forms of tACS

2.2.1 Stimulation waveforms

Three conventional/quasistatic and three non-quasistatic tACS methods were studied (Figure 2). The conventional methods comprising a single quasistatic E-field included 10 Hz low frequency stimulation (LFS), 2 kHz high frequency stimulation (HFS), and 2 kHz AM-HFS with 10 Hz modulation. Non-quasistatic methods included TIS (two E-fields with 2 kHz and 2.01 kHz frequency, respectively), rotational field HFS (RFS, two E-fields with 2 kHz frequency and a 90° phase shift) and AM-RFS (RFS with 10 Hz-modulated E-fields), which were all simulated with E-field amplitude ratios of 1:1, 2:1, 4:1. RFS was studied to examine how the field rotation alone affects tACS, and AM-RFS was included to examine how non-interference-generated AM compares with AM of TIS. The waveforms had a duration of 4 s and, to reduce onset response, 0.5 s and 0.25 s linear ramp-up and ramp-down at the beginning and end, respectively.

2.2.2 Realistic neuron model

To capture fully the effect of TIS, RFS, and AM-RFS on 3D cortical neurons, we used neuron models from the Blue Brain project [47,48] that were previously adapted and validated for stimulation with extracellular E-fields [31,42]. The models were implemented in the NEURON v7.4 [49] and included cell-type specific 3D dendritic and axonal morphologies reconstructed from juvenile rat brain slices and up to 13 Hodgkin-Huxley-like ion channel types. Key modifications included myelinating the axons, scaling ion channel kinetics to body temperature, and assigning ion channel properties to the entire axon arbor [42]. Layer 5 (L5) pyramidal cells (PC, Figure 3A) were simulated as they have the largest size and thus lowest thresholds in response to extracellular stimulation [31,42]. The main axon's terminal was disabled from direct activation by extracellular stimulation to account for the truncation of the main axons in the slicing process and the artificial creation of these low threshold sites [31]. To

capture better the response to kHz stimulation and match more recent studies of axonal excitability [50,51], the kinetics of the sodium channels were accelerated by uniformly scaling the time constants of the gating variables of the fast sodium channel (m^3h) by 0.4 for both the activation (m) and inactivation (h) gates. The overall effect was a faster firing rate in response to intracellular stimulation, and a decrease in thresholds to kHz stimulation (in the range of −20% to −12.5%) with limited effects on LFS (Figure S1). We conducted simulations of all stimulation parameters with one representative L5 PC model, and confirmed that the findings are generalizable across cell morphologies using simulations of a subset of parameters in four additional model clones (Figure S2). We also tested the thresholds of a L2/3 PC model and a L4 large basket cell model (Figure S2), but we did not carry out more extensive characterization of these cell types since their thresholds were significantly higher than those of the L5 PCs for both low and high frequency stimulation.

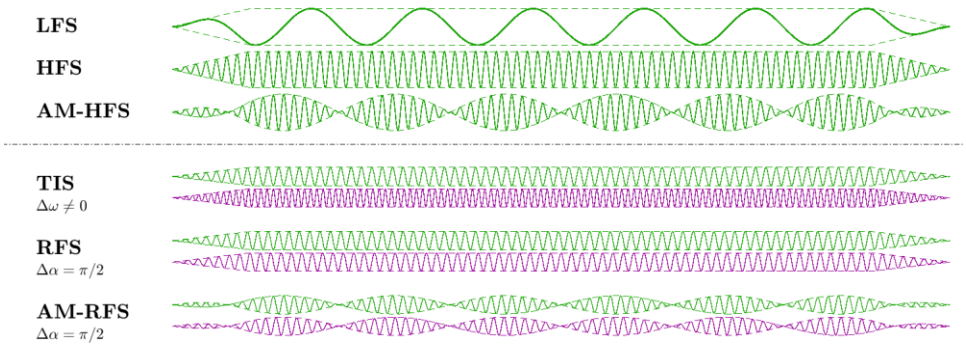

Figure 2. Stimulation waveforms of various tACS modalities

Illustration of the waveforms of low frequency stimulation (LFS), high frequency stimulation (HFS), amplitude-modulated HFS (AM-HFS), temporal interference stimulation (TIS), rotational field HFS (RFS), and amplitude-modulated RFS (AM-RFS). The waveforms of the conventional methods and the first E-field of non-quasistatic stimulation methods are shown in green, and the waveform of the second E-field of non-quasistatic stimulation methods are shown in purple. The envelope of all waveforms is shown with dashed lines and has a ramp-up and ramp-down period. The relative frequencies are for visualization and not to scale with the actual stimulation.

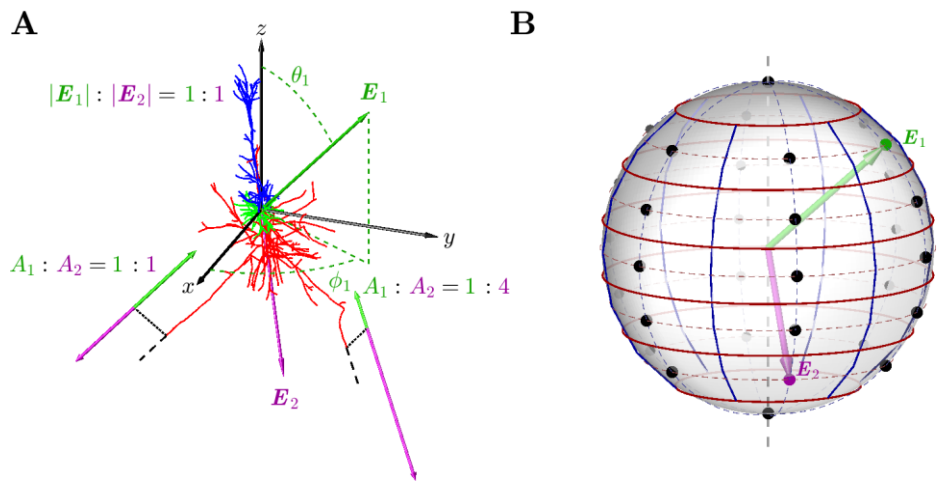

Figure 3. Neuron model and definitions of E-field orientation

A. L5 PC morphology and the spherical coordinate system for E-field orientation. The origin is located at the soma with the *z*-axis aligned along the somatodendritic axis. The E-fields are defined by their polar and azimuthal angles, θ and ϕ, shown for the first E-field (green) as example. The E-fields have different effective amplitudes (A_1, A_2) at different locations along the neural cable, as shown at two terminals in the axonal arbor, with the black dashed lines showing the orientation of the axon at the terminals. Color legend for neuron: apical dendrite in blue, basal dendrite in green, and axon in red. **B.** Sampling of 32 E-field orientations for the 3D neuron model represented by dots on a spherical surface, with black and grey dots indicating the front and back of the sphere. The polar axis is shown as a vertical dashed line.

2.2.3 Simulation setup

The orientations of the E-fields were defined in a spherical coordinate system centered at the soma and with the polar direction (*z*-axis) aligned with the somatodendritic axis (Figure 3A) [42]. Given the alignment of the somatodendritic axis with the cortical column, the polar angle reflects the orientation of the E-field relative to the cortical geometry and more significantly influences activation thresholds, whereas the azimuthal rotation of neuron models within the cortex are random [31]. To achieve a uniform representation on the spherical surface, the 32 E-field orientations were taken from a grid of seven non-uniformly sampled polar angles and six uniformly sampled azimuthal angles (Figure 3B). For stimulation methods comprising two E-fields, both fields were sampled with the

32 orientations, yielding a total of 1024 (32 × 32) orientation combinations for each parameter setting (i.e., frequency, amplitude modulation, phase shift, and amplitude ratio). NEURON's extracellular mechanism [42,49] was used for coupling the E-fields to the models, with the extracellular potential V_e for each compartment c calculated as

$$V_{\mathrm{e},c}(t) = \left(\boldsymbol{E}_1(t) + \boldsymbol{E}_2(t)\right) \cdot \boldsymbol{l}_c \quad ,$$

where $\boldsymbol{l}_c$ is the displacement vector specifying the compartment location relative to the soma. The simulations were set up in MATLAB (versions 2019a and 2020a, The Mathworks, Natick, MA, USA) and performed in NEURON with a time step of 10 µs, which was sufficient to capture the approximately 0.5 ms period of the kHz stimulation and the response of the fast sodium channels with fastest time constant of ~ 40 µs.

The threshold for activation was defined as a response with a firing rate of at least 9.5 Hz at the soma, which is 95% of the 10 Hz frequency of LFS, the difference frequency of TIS, or the frequency of the amplitude modulation (Figure 4A). Bursting was defined as spiking events with less than 15 ms inter-spike intervals within a 50 ms duration [16]; if bursting occurred, the bursts were counted instead of individual spikes to calculate the firing rate in the threshold search. Only spikes within the steady state period of the stimulation were counted, and onset or offset response during the ramp-up and ramp-down time was not considered for threshold determination. Therefore, a suprathreshold response should have at least 31 spikes or bursts during the steady state stimulation period. Setting the threshold firing rate to a slightly lower value allowed the neuron's activity to better mimic experimental recordings, in which some trials did not result in firing during every cycle of the LFS or TIS envelope [16]. Threshold amplitude was determined by a binary search to 1% accuracy and, for non-quasistatic stimulation methods, was defined as the maximum amplitude of the total E-field. To determine whether action potentials were initiated in the soma or axons, we compared the spike timing at several compartments, namely the soma, axon initial segment, first node of the axon (directly connected to the initial segment), and terminal of the main axon.

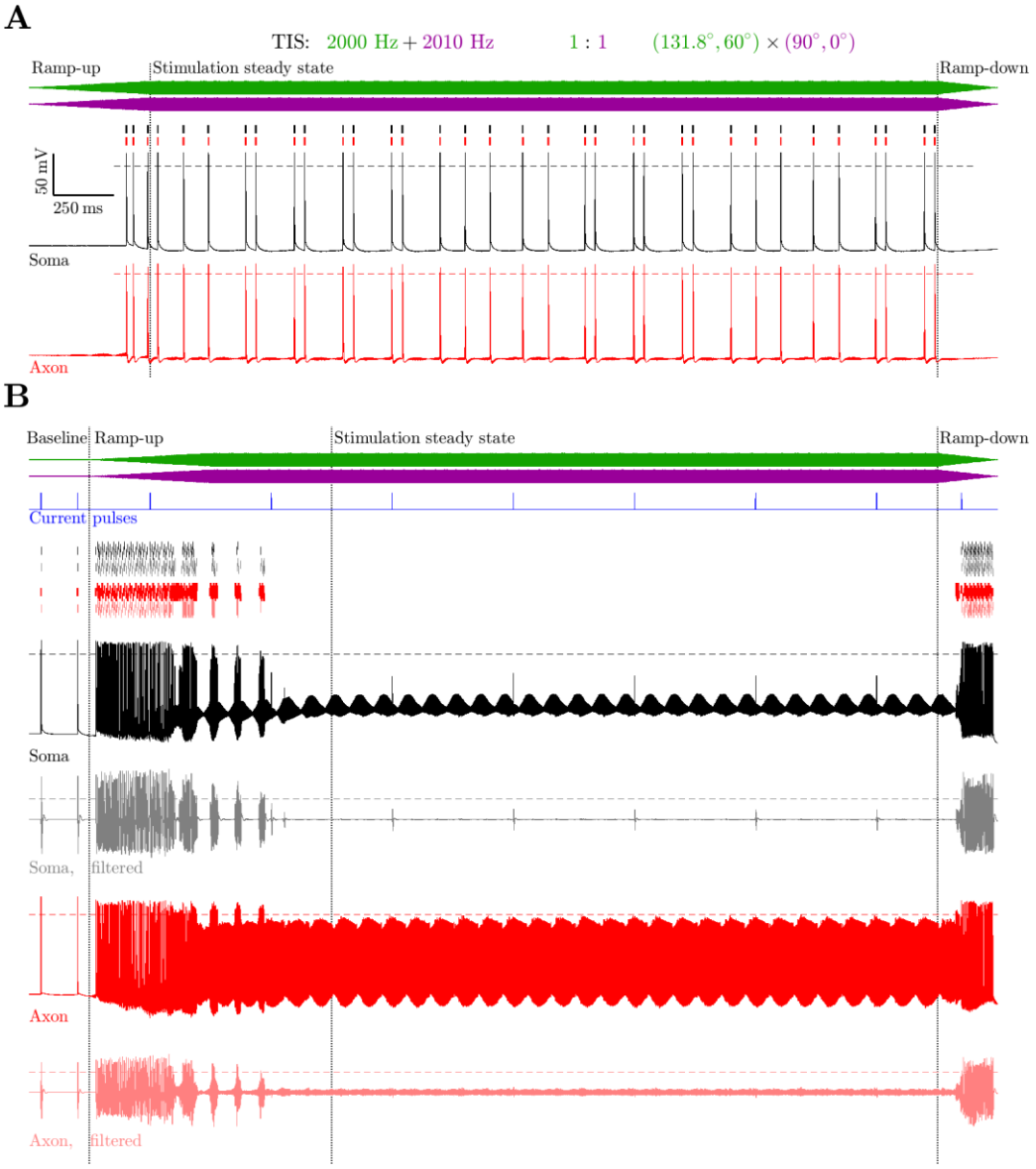

Figure 4. Neural response and neural recording processing

A. Example response of L5 PC firing in response to TIS at threshold. The stimulation waveforms of the two E-fields are shown on top, followed by raster plots of firing and transmembrane potentials for the soma (black) and an axon node (red). Individual spikes or the first spike within a burst are aligned horizontally, with additional spikes within a burst offset vertically. The dotted vertical lines mark the start and end of the stimulation steady state period between 0.5 s and 3.75 s, and the horizontal dashed line marks the spike thresholds. **B.** Example response of L5 PC conduction block in response to TIS at high amplitude. Suprathreshold intracellular current pulses (blue) were applied to the soma and evoked action potentials at baseline. However, they did not evoke action potentials during

the stimulation steady state, either in the raw (black) or filtered (grey) membrane potential. The membrane potential deflection in the soma generated by the test current pulse did not generate action potential in the axon (red traces). The dotted vertical lines mark the baseline period ending at 0.25 s and start and end of the stimulation's steady state period between 1 s and 3.75 s.

Thresholds for conduction block [23] were determined to examine whether the non-quasistatic stimulation methods could generate high frequency block. Suprathreshold test current pulses were injected into the soma to examine transmission of action potentials. The start of waveforms was therefore delayed by 0.25 s to allow test pulses to be applied during baseline. To further accommodate the strong onset response, the steady state was considered to start 0.25 s after the ramp ended. Therefore, the period for which action potentials were considered for conduction block was 2.75 s, starting 1 s after the stimulus onset. The threshold search was terminated and "no block" was determined for a particular set of stimulation parameters when the maximum tested amplitude of the (first) E-field reached 6000 V/m and action potentials were still occurring during the steady state stimulation period. This upper limit was chosen as an arbitrarily high E-field value well above the stimulation threshold and about three times the lowest block threshold observed in the simulations. To match the filtering applied to patch clamp recordings of cortical and hippocampal neurons [16], the membrane potential was filtered using a 5th order band stop filter (1 kHz to 15 kHz) and a 3rd order high pass filter (100 Hz). This removed the stimulation "artifact" due to the high stimulation amplitude directly driving the neural membrane above the 0 mV threshold, revealing the underlying action potentials (Figure 4B). Firing patterns were compared for both the raw and filtered transmembrane potential, with a 25 mV threshold used for the latter.

3 Results

3.1 Firing pattern and threshold of activation

For all tACS methods and across all E-field orientations or orientation combinations, spiking events occurred earliest in the first node of the axon. As axon terminals had the lowest thresholds to extracellular stimulation [42,52], the responses were all initiated in the axonal arbor and propagated antidromically to the soma and re-orthodromically through the main axon [31,42].

At threshold, the firing patterns evoked by all stimulation modalities showed a response before the E-field oscillations reached steady state amplitude (Figure 5), and this was not eliminated by the ramp-up of the E-fields. For LFS, AM-HFS, and AM-RFS, the responses during stimulation steady state were single spikes at regular intervals corresponding to the frequency of the stimulation or amplitude modulation, and the early spikes were part of this regular firing. For HFS, TIS, and RFS, the bursts of activity before stimulation reached steady state appeared to be a transient onset response. During steady state stimulation, the HFS and RFS responses consisted of short patterns of two spikes that repeated regularly but did not satisfy the definition of bursts. The TIS responses exhibited regular firing at the difference frequency for most E-field orientation combinations, and changing the amplitude ratio had negligible effect on the firing pattern. For some orientation combinations, the firing pattern was irregular and exhibited bursts consisting exclusively of double spikes. For TIS with a 1:1 E-field amplitude ratio, bursting occurred in 229 of the 1024 orientation combinations of the E-fields. In orientation combinations where bursts occurred, bursting accounted for 3.2 ± 0.1% of firing events (mean ± standard deviation), whereas among firing events across all orientation combinations, only 0.7% were bursts. Increasing the E-field amplitude ratio to 2:1 and 4:1 reduced both the number of orientation combinations evoking bursting and the number of bursts (181, 3.2 ± 0.1%, and 0.6%, and 78, 3.3 ± 0.1%, and 0.2%, respectively). While only TIS evoked bursting at threshold, the neuron model could respond with bursting to suprathreshold stimulation amplitudes for all stimulation modalities (Figure S3).

Activation thresholds were significantly lower for LFS (range 16.9 V/m to 47.4 V/m) compared to all kHz tACS modalities (Figures 6 and S4–S8), as expected due to the low-pass filtering by the neuronal membrane [23,28]. The kHz tACS thresholds all fell within a similar range (75 V/m to 230 V/m) despite some variation in their distributions. Thresholds varied with the E-field orientations (Figures S5–S8). Due to the oscillation of the E-fields, the threshold maps were symmetric for points corresponding to E-fields of opposite orientations. The lowest threshold orientation for LFS was aligned with an axon collateral, whereas the lowest threshold for kHz tACS was aligned with the somatodendritic axis. For TIS, RFS, and AM-RFS, the thresholds mostly increased with the E-field amplitude ratio (Figure S4). The change was less prominent for TIS due to the response being dominated by the first E-field, and this also resulted in clustering of the thresholds for unequal E-field amplitudes (Figures 6).

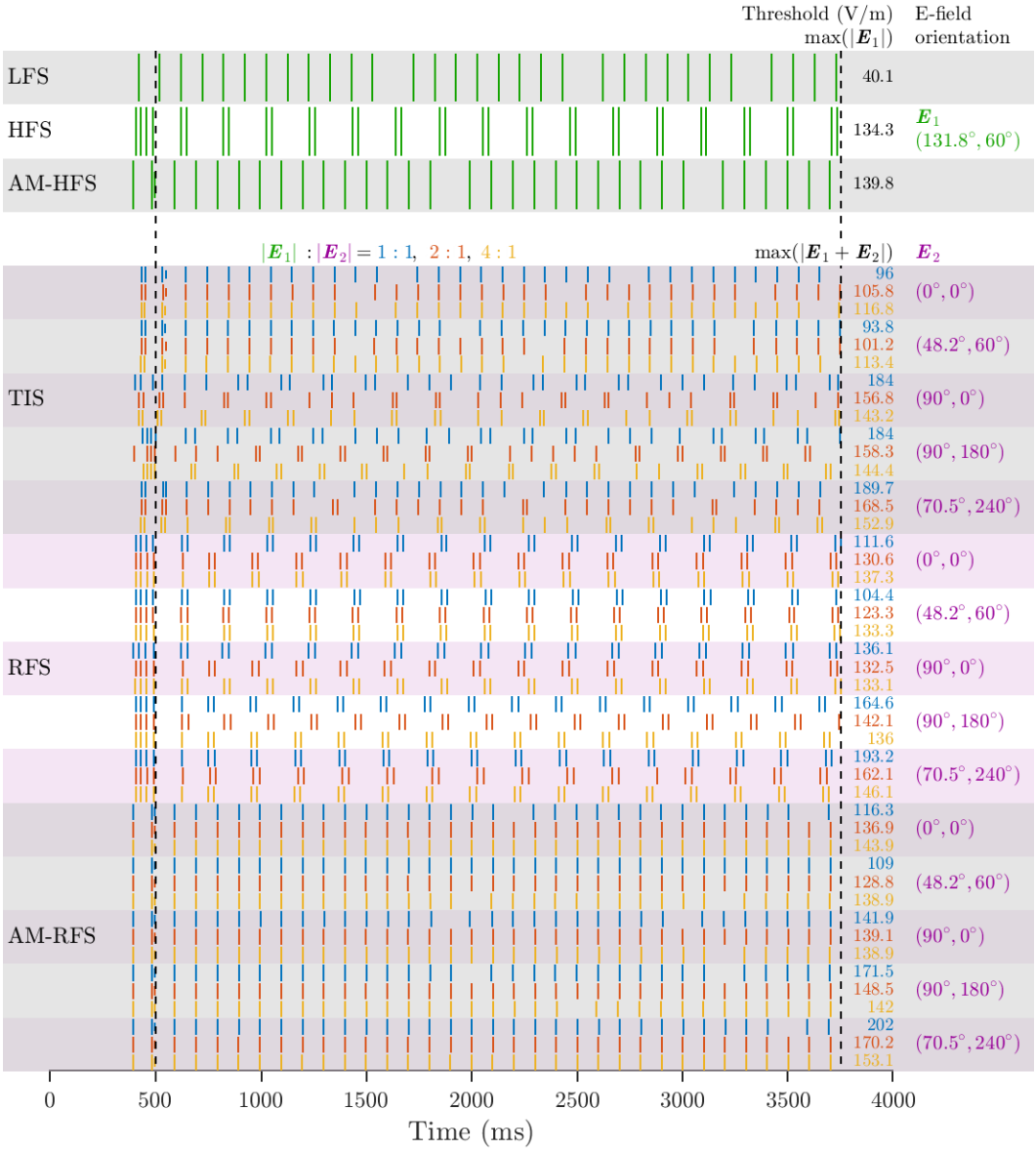

1 **Figure 5. Representative responses of L5 PC at activation threshold**

2 Raster plot of somatic firing. The same orientation was chosen for the E-field of LFS, HFS, and AM-HFS as well
3 as for the first E-field of TIS, RFS, and AM-RFS. The same five orientations were chosen for the second E-field of
4 TIS, RFS, and AM-RFS, with results for all 3 amplitude ratios of the two E-fields shown (from top to bottom: 1:1,
5 2:1, 4:1 in blue, red, and yellow, respectively). The dotted vertical lines mark the start and end of the stimulation
6 steady state period between 0.5 s and 3.75 s.

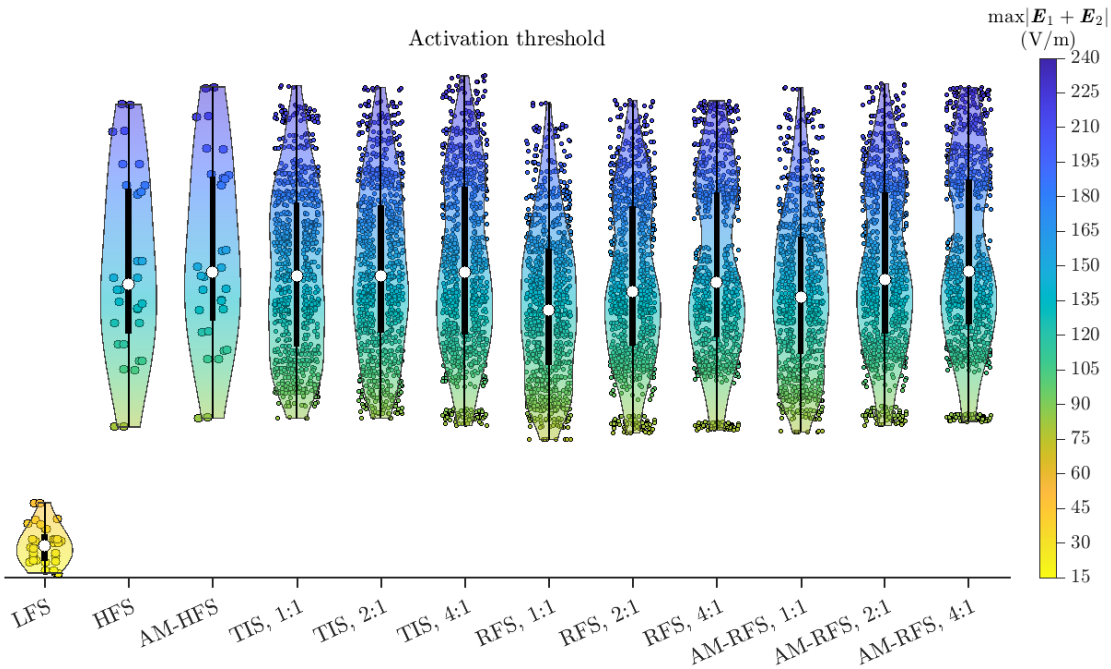

Figure 6. Activation thresholds

Thresholds for action potential generation for all 32 orientations (LFS, HFS, and AM-HFS) and 1024 orientation combinations (TIS, RFS, and AM-RFS) of E-field(s). Each violin plot shows the individual data points as circles (with jitter fixed for the E-field orientations and orientation combinations), the estimated density of distribution as a shaded area, and several statistics as box-and-whisker, with the white circle representing the median, the box covering the first to third quartiles, and the whiskers extending to the upper and lower adjacent values that are 1.5 times the interquartile range above and below the quartiles.

3.2 Firing pattern and threshold of conduction block

At sufficiently high E-field amplitudes, all kHz tACS modalities evoked a strong onset response during ramp up and an offset response during ramp down (Figures 7, 8, and S9). For the majority of E-field orientations of HFS, TIS, and RFS, conduction block could occur during the stimulation steady state for E-field amplitudes within the maximum tested amplitude (Figures 9 and S10–S14). For all AM-HFS and AM-RFS cases, periodic activation at the frequency of amplitude modulation occurred for all suprathreshold E-field amplitudes. At low stimulation amplitudes, the activation coincided with the maxima of the AM envelope. At high amplitudes, however, the

activation shifted to the minima of the envelope, indicating the activation was an onset/offset response separated by conduction block during periods of high E-field amplitude (Figure S14A and S14C). Similarly, when sustained block was not observed for TIS, the bursts of firing were shifted by half the modulation period relative to the burst activation at lower field strengths, and the neural membrane was blocked between the onset and offset responses (Figures $8B_{ii}$).

Block thresholds had a wide distribution (Figure 9) and were strongly dependent on E-field orientation (Figures S10–S13). Block thresholds for TIS decreased with increasing E-field amplitude ratio, and, except for 4:1, were higher compared to HFS and RFS. For TIS with equal E-field amplitudes, neurons were more likely to be exposed to a total E-field with stronger low-frequency modulation (Figure 3A), which generated periodic onset and offset responses interrupting the block. On the other hand, for unequal E-field amplitudes, the modulation was weaker and therefore could achieve block at lower threshold. Block thresholds for RFS increased with amplitude ratio and were similar to HFS. For RFS, equal E-field amplitude exposed more axon terminals to higher aligned E-field at the kHz frequency, resulting in block at lower thresholds. In contrast, some axon terminals were aligned with the weaker E-field of the unequal E-fields, resulting in higher block thresholds.

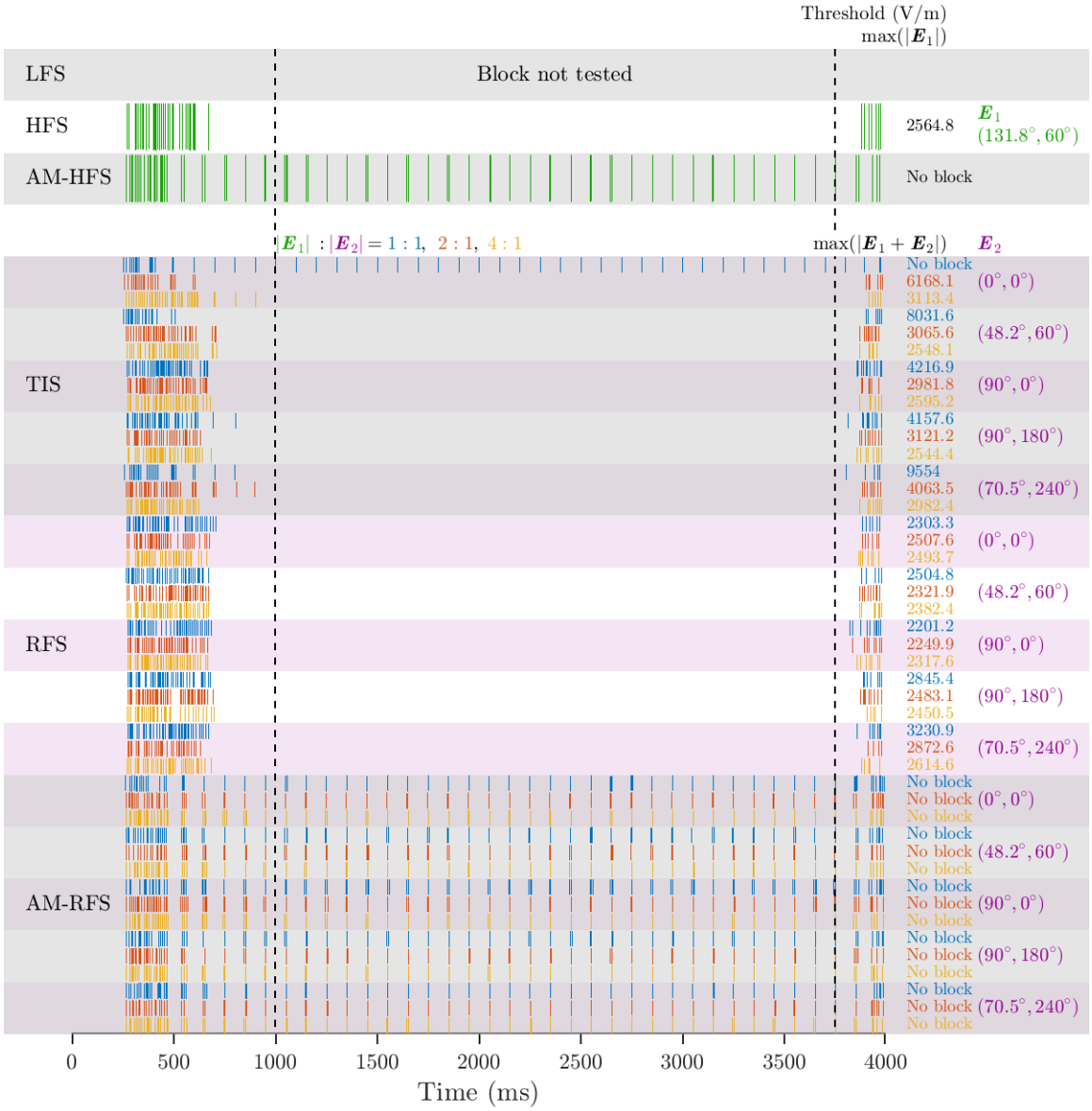

Figure 7. Representative responses of L5 PC at conduction block thresholds or maximum amplitude tested

Raster plot of somatic firing for the same E-field orientations as in Figure 5, showing the spikes of the filtered transmembrane potential of the soma. Same results for spikes of the raw transmembrane potential are shown in Figure S8.

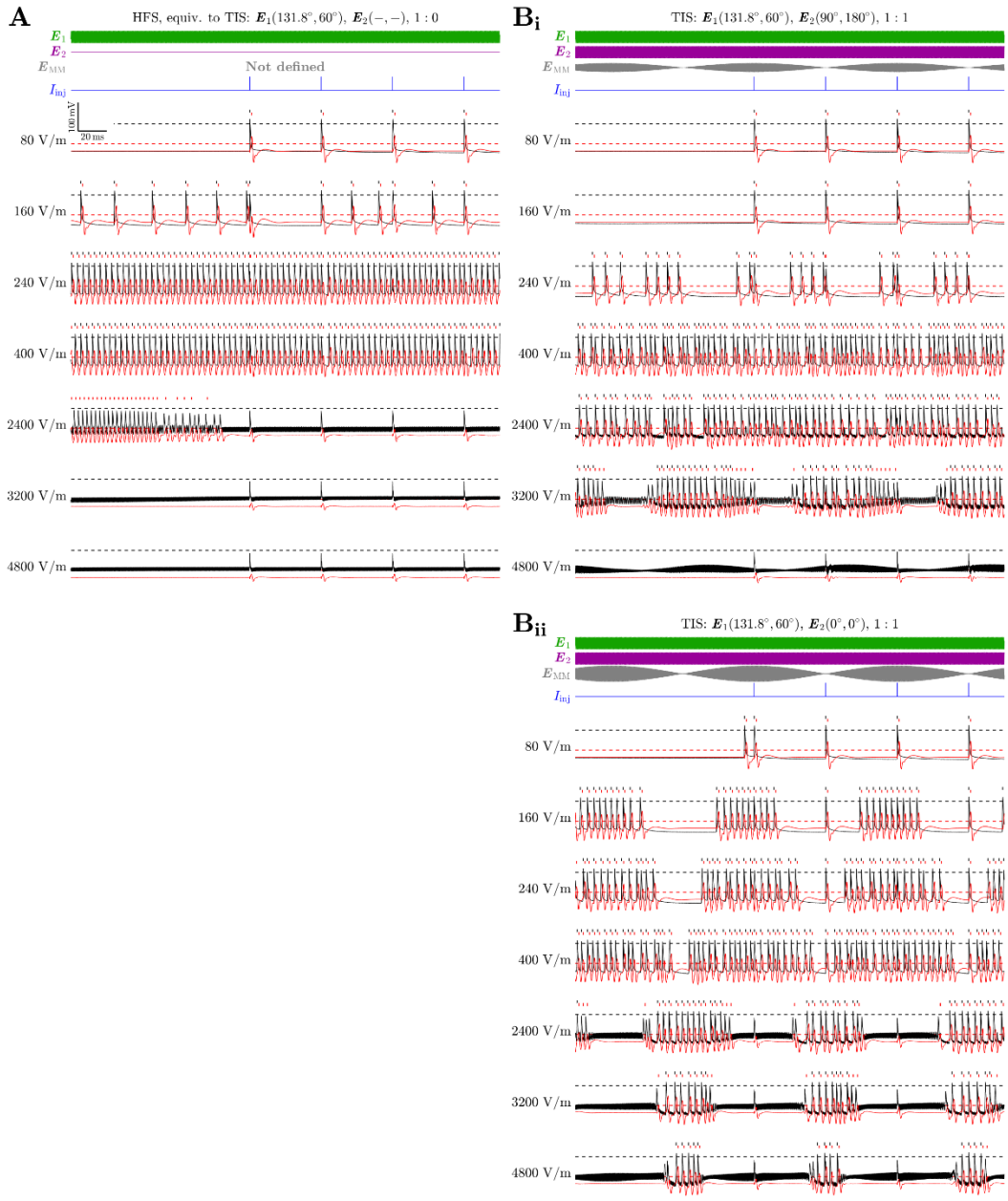

Figure 8. Representative neuron firing evoked by HFS and TIS for a range of E-field amplitudes

The raw (black) and filtered (red) transmembrane potential at the soma with action potential timing marked with vertical lines for seven different E-field amplitudes given on the left as either max($|\boldsymbol{E}_1|$) for HFS or max($|\boldsymbol{E}_1+\boldsymbol{E}_2|$) for TIS. The dashed lines show the action potential threshold of 0 and 25 mV for the raw and filtered transmembrane potentials, respectively. Shown on top are the individual E-field waveforms (green and purple), total E-field along the direction of maximum modulation ($\boldsymbol{E}_{\mathrm{MM}}$, gray), and timing of suprathreshold current injection test pulse (I_{inj},

blue). The orientation of the (first) E-field is the same as in Figures 5 and 7, and two orientations of the second E-field are shown. **A.** HFS, which is equivalent to TIS with 1:0 amplitude ratio, evoked sustained firing with increased E-field amplitude and resulted in conduction block at high stimulation amplitudes. **B.** TIS evoked periodic firing at lower amplitudes, which became sustained firing similar to HFS at higher amplitudes, and then became periodic again at even higher amplitudes as the amplitude modulation of the total TIS E-field resulted in onset and offset firing. Depending on the E-field orientations and corresponding amplitude modulation of the total E-field, the onset/offset firing may cease (**B**$_{\mathbf{i}}$) or persist (**B**$_{\mathbf{ii}}$) at higher E-field amplitudes, but the transmembrane potential reached a blocked state and did not respond to stimulation. Results for AM-HFS, RFS, and AM-RFS are shown in Figure S14.

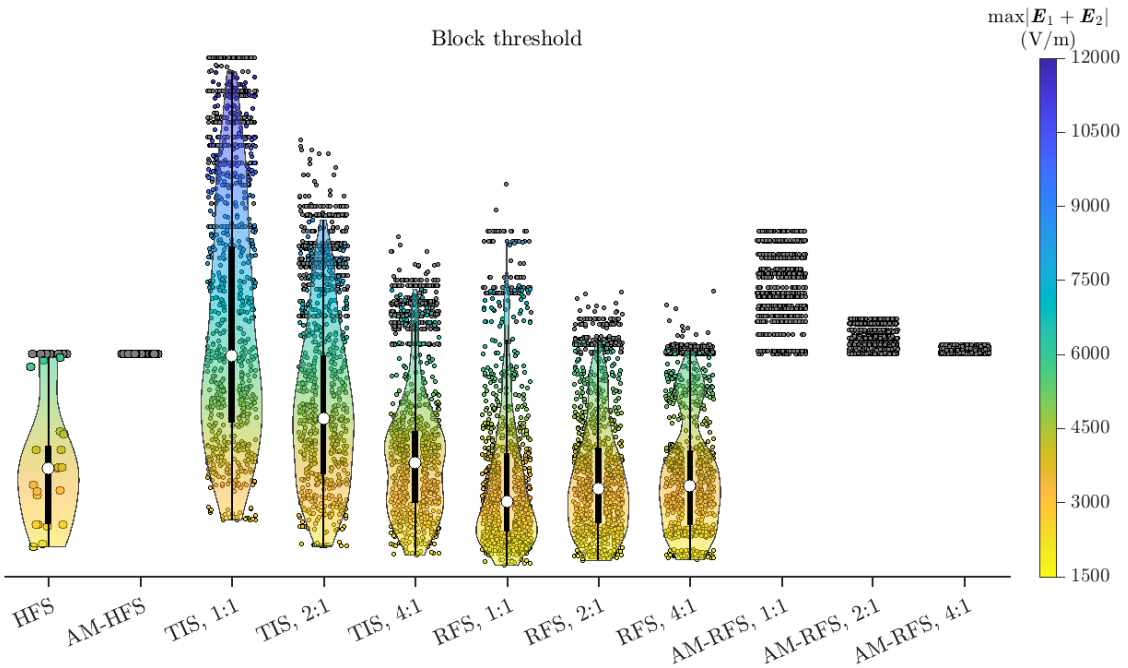

Figure 9. Conduction block threshold

Thresholds for all 32 orientations (HFS and AM-HFS) and 1024 orientation combinations (TIS, RFS, and AM-RFS) of E-field, in a format similar to Figure 6. Orientations (combinations) that did not achieve block with $|\boldsymbol{E}_1| \leq 6000$ V/m are shown as grey circles.

4 Discussion

4.1 Characteristics of TIS

We quantified the activation and conduction block of model L5 PCs by single channel tACS (10 Hz LFS, 2 kHz HFS, and 10 Hz modulated 2 kHz AM-HFS) as well as methods for modifying the spatial selectivity of tACS using two high-frequency currents to generate E-field temporal interference with two closely spaced frequencies (2 kHz + 2.01 kHz TIS) or E-field rotation through relative phase shift without or with amplitude modulation (2 kHz RFS and 10 Hz modulated 2 kHz AM-RFS). TIS evoked periodic activation of the model neurons at the difference frequency of the two stimulation currents, similar to prior results [16]. Unlike the experimental results, however, TIS thresholds were comparable to those of HFS, as well as those of RFS or their AM versions. In our models, the E-field amplitudes to achieve activation across all forms of kHz tACS (75 to 230 V/m) were much higher than the range for LFS (16.9 to 47.4 V/m). At markedly higher amplitudes (> 1700 V/m), neuronal responses and endogenous activity could be blocked by non-modulated kHz tACS, including TIS. While TIS did generate amplitude modulation of the total E-field projected locally along the neural cables, its depth of modulation and magnitude of the modulated waveform were highly dependent on the amplitude ratio of the two E-fields as well as their orientations with respect to the neural cable. Therefore, the E-field projected on the neural cables has smaller magnitude and shallower modulation compared to the maximum values determined by the TIS E-fields alone. Consequently, TIS generates conduction block similarly to regular kHz stimulation without modulation, whereas AM-tACS with maximum modulation depth cannot generate block for any E-field direction.

Our study related neuronal responses to the strength and temporal characteristics of the local E-field. To link the transcranially applied stimulus current with the E-field, Rampersad et al. [35] simulated the E-field in a mouse brain with a model representing the conditions of the original study [16]. They reported TIS E-field maximum of 383 V/m, higher than the threshold E-field values in our study. However, their E-field was defined for the amplitude of the envelope along the orientation of maximum modulation [16,35]

$$E_{\mathrm{TIS}}^{\mathrm{max.mod.}} = \begin{cases} 2 \cdot \min(|\boldsymbol{E}_1|, |\boldsymbol{E}_2|) & \text{if } |\boldsymbol{E}_1||\sec(\beta)| < |\boldsymbol{E}_2| < |\boldsymbol{E}_1||\cos(\beta)| \\ |(\boldsymbol{E}_1 + \boldsymbol{E}_2) \times (\hat{\boldsymbol{n}}_1 - \hat{\boldsymbol{n}}_2)| & \text{otherwise} \end{cases},$$

where $\beta \in [0, \pi]$ is the angle between the two E-fields and $\hat{\boldsymbol{n}}_{1,2}$ are unit vectors along the E-fields. The E-field along the maximum modulation orientation does not reflect the maximum E-field, $\max|\boldsymbol{E}_{\mathrm{TIS}}(t)|$, over an entire low frequency period of TIS and, in general, is smaller than the latter (Figure 1B). A metric comparable to our reported thresholds is the maximum E-field amplitude of conventional two-channel tACS with the same combination of E-field orientations and amplitude ratio, which was 38,000 V/m [35]. This value is much higher than our activation thresholds and an order of magnitude higher than the conduction block thresholds. The model by Rampersad et al. did not include the skin, and such high E-field amplitude compared to other studies [37] may be attributed to the absence of current shunting by conductive soft tissues [7]. Nevertheless, even if Rampersad et al. overestimated the E-field by tenfold, our simulation results indicate that TIS applied epicranially to mice could achieve conduction block in cortical neurons, similar to previous computational studies that examined the effects of TIS on peripheral axons [23]. Therefore, the periodic activation observed *in vivo* in mouse experiments may reflect onset responses of nerve block in the target region, in which the block was released periodically due to amplitude modulation of the TIS E-field, whereas the surrounding area was completely blocked due to much smaller modulation.

In humans, however, tolerable tACS currents for scalp stimulation without anesthesia are only a few mA and generate E-fields in the brain of only 0.1 V/m to 1 V/m [8,38]. While these E-field amplitudes are sufficient to modulate neural activity [17,53–55], they are orders of magnitude lower than both activation and block thresholds of TIS. Our modeling results indicate that suprathreshold TIS would require E-fields in the range from 150 V/m to 800 V/m, corresponding to scalp electrode current of hundreds of mA to over 1 A, which is comparable to or exceeds that in electroconvulsive therapy (ECT) [56,57]. Therefore, the generation of suprathreshold TIS effects would be intolerable without anesthesia, could result in heating at the electrode–scalp interface, and may induce a seizure with continuous application. Nevertheless, subthreshold TIS [30,32], which involves very different mechanisms, may still merit investigation due to the unique properties of the TIS E-field. Likewise, TIS could be of interest in suprathreshold applications under anesthesia in the context of ECT or intensive nonconvulsive stimulation [58].

Our results revealed complexities of the E-fields produced by TIS and RFS that have implications for the design and interpretation of modeling and experimental studies. The activation and block thresholds for the E-fields of

these non-quasistatic stimulation methods varied not only with their amplitude ratio and angle but also with their orientations relative to the neuron morphology. For example $\boldsymbol{E}_1$ and $\boldsymbol{E}_2$ with given polar angles (θ_1 and θ_2) and co-varying azimuths ($\varphi_1 - \varphi_2$ = constant) span a fixed angle, but the thresholds vary significantly (Figure S6–S8 and S12–S13). Therefore, the E-fields obtained along specific directions in computational models, whether for maximum modulation [15] or in a pre-determined orientation [16,35,36], cannot predict the stimulation effects of TIS, and optimization using calculation of the E-field alone [34,59] is unlikely to produce the same results as when considering the effects of the E-field on neurons.

Further, TIS has unique features compared to the other kHz stimulation methods that were tested. TIS creates amplitude modulation in the target region, i.e., the region where the two E-field amplitudes are similar. The slight differences between the TIS waveforms for aligned E-field compared to that of a single channel kHz AM-tACS could have non-negligible effects on neural activation. TIS also creates rotational E-field where the two E-field orientations are not directly aligned, and this generally includes the target region as the two pairs of electrodes are placed on opposite side of the head. In contrast, the E-field of conventional AM-tACS contains no rotation and would only engage a subset of the neural targets recruited by TIS, despite being able to achieve larger modulation depths for a given orientation [15]. The rotation of TIS is emergent due to the varying phase difference during the low frequency cycle, whereas the magnitude of rotation of RFS is sensitive to the phase difference between the waveforms applied at the two pairs of electrodes. In non-target regions, the TIS E-field is mostly oscillatory with minimal rotation and amplitude modulation. This results in similar activation thresholds to HFS and could result in conduction block at high field amplitudes, where higher amplitude ratios would confer lower block thresholds than in the target region. Of the methods capable of producing conduction block, TIS also has the highest block thresholds. AM-HFS and AM-RFS cannot achieve conduction block, whereas RFS achieves block at lower thresholds for equal E-field amplitudes compared to unequal amplitudes. On the network level, the asynchronous variation of the TIS E-field over space should be considered [43]. Therefore, experiments such as brain slice studies should consider replicating the features of the TIS E-field with either two stimulation channels or a simultaneously amplitude- and frequency-modulated E-field, rather than substituting it with a single-frequency AM E-field [32].

4.2 Filtering of membrane potentials

We analyzed the neuronal responses based on the raw transmembrane potential recordings to determine activation thresholds. At threshold E-field amplitudes, the kHz oscillations of transmembrane potential had limited amplitudes (5 mV to 15 mV) throughout the cell and did not mask the action potentials. Thus, spike analysis for determination of activation thresholds did not require filtering. For conduction block, the transmembrane potential could be driven beyond 0 mV (or another arbitrarily defined threshold) by kHz waveforms at high amplitudes. These high amplitude oscillations are "real" and not artifacts, making it difficult to distinguish action potentials which ride on top of or are merged with these oscillations. Spikes could nevertheless be identified by temporal or frequency features, as transmembrane potential oscillations of blocked neurons were sinusoidal and removed by filtering, while spikes resulted in distortions that remained after filtering.

In experimental studies of neural stimulation, electrophysiological recordings are contaminated by stimulus artifacts, e.g., the kHz extracellular E-field in TIS. Not only is filtering often necessary as a post-processing step, multiple filters are integral components of the experimental rig before the data are sampled [60]. In [16], the current clamp traces were band-stop filtered (1 kHz and 15 kHz) and high-pass filtered (100 Hz). While the neurons themselves were unlikely to fire at frequencies over 100 Hz in response to stimulation, it was unclear whether the filtering resulted in the loss of some spikes for the kHz frequency stimulation and TIS. It appears that spikes could be identified from TIS and HFS only when the artifact amplitude was relatively small and spikes were visible even in the unfiltered traces, i.e., during the initial ramp-up time for both TIS and HFS and during each ramp-up of the low frequency envelope of the TIS waveform [16]. During the steady state of HFS and near the peak of the low frequency envelope of TIS, spikes that were overwhelmed by the artifact could have been lost due to the filtering, leading to a conclusion that there was no response to HFS. As such, alternate artifact removal strategies could be pursued, such as subtraction of an artifact template, or using an ideal notch filter in the frequency domain. Neuronal models are not limited by such artifacts and allow direct access to the transmembrane potential. While advantageous for data analysis, filtering of simulated membrane potentials should be performed with caution as it complicates the interpretation of modeling results and their comparison with experimental studies.

4.3 Limitations

Our simulations examined the neuronal response to uniform E-fields under the quasi-uniform approximation for transcranial stimulation. Due to this simplification, the thresholds could not be directly correlated with current amplitudes applied to tACS electrodes, and the spatial distribution of neural activation within the cortex was not determined. Nevertheless, simulations of E-field distributions in realistic head models can easily fill this gap, whether using a multiscale model with neuron models embedded in the cortex [31] or applying the cortical E-field to the uniform field results in our study [41,61]. Therefore, the E-field orientation combinations and their amplitude ratios in this study are representative of neurons at different cortical locations.

Despite their realistic morphologies and complexity of ion channels, the model neurons have limitations capturing the response to high frequency stimulation. For extracellular stimulation, axon terminals are the sites of action potential initiation due to their sensitivity to E-fields [42,52]. However, channel conductances and dynamics are not readily available for the axonal arbor beyond the initial segment and have to be inferred from the parameters of the soma. This may contribute to simulated transcranial stimulation thresholds being on average about two fold higher than experimental data, although the simulated and experimental threshold distributions overlap [31]. Further, the sodium ion channel dynamics were fitted to recordings from patch clamp recording [62], which could underestimate the kinetics of axonal sodium channels due to filtering (2 kHz low pass filter) and recording below body temperature (24°C). We accelerated the fast sodium channels that contribute the most to action potential firing to capture better the response to kHz stimulation; however, further improvements are required to increase the accuracy of cortical neuron models. Nevertheless, analyses of transcranial stimulation should use cortical neuron models with realistic myelinated axonal morphology at body temperature, and classic Hodgkin-Huxley channels [63,64] are ill suited to transcranial stimulation studies.

We did not include intrinsic activity or network connectivity in this study. Although patch clamp recordings in the anesthetized mice exhibited negligible spontaneous firing (< 0.5 Hz) [16], intrinsic subthreshold fluctuation of the transmembrane potential could have interacted with the exogenous E-field. However, threshold changes for stimulation during the afterpolarization of an action potential is on the order of ±50% [65], and therefore

transmembrane potential fluctuations alone are unlikely to account for the discrepancy of threshold differences between LFS and kHz tACS when comparing the experiments and our simulations.

As our goal was to explore the hypothesis of single-neuron demodulation of TIS, we did not include synaptic connections between neurons, and network modulation could be a potential mechanism for TIS. While network activation can be advantageous and exploited to reach deep targets or to improve stimulation efficacy, for example using TMS to modulate the hippocampus, midbrain, or subgenual cingulate by stimulating functionally-connected cortical areas [66–69], it could also be considered a limiting factor on the focality of transcranial stimulation methods, including TIS. For example, Grossman et al. [16] used c-Fos immunochemistry to demonstrate activation of the hippocampus without activating superficial cortical areas, with strong c-Fos immunoreactivity in the entire region of granule cells within the dentate gyrus. This expression was much stronger than observed anywhere for LFS or elsewhere in TIS, suggesting that TIS achieved strong synchronous activation of the local circuitry in the dentate gyrus that could potentially be a result of focal seizure. Furthermore, the area of activation indirectly inferred based on immunohistochemistry does not correlate with the distribution of the simulated E-field modulation envelope amplitude [16], complicating the interpretation of the mechanism and focality of TIS. While these limitations are important directions for future refinement of the models, they would affect similarly TIS and the other forms of kHz stimulation. Therefore, our conclusions regarding the relative effects and thresholds across these modalities appear unlikely to be significantly altered.

5 Conclusions

We analyzed the E-field characteristics of TIS and quantified the responses of model cortical neurons to suprathreshold TIS and related kHz tACS modalities. The analysis revealed unique spatiotemporal characteristics of the TIS E-field, including phase-shift and frequency jitter of the TIS waveforms due to the difference in E-field amplitudes for aligned E-fields, as well as rotation of the total E-field for non-aligned E-fields. These findings highlight the importance of representing the TIS E-field in 3D and using morphologically-realistic neuron models. TIS had activation thresholds similar to other kHz tACS modalities and much higher than those of low frequency tACS. As expected, the bursts of activation evoked by near-threshold TIS were synchronized with the maxima of

the low frequency modulation envelope of the total E-field, providing one possible mechanism for the previously reported experimental responses. Further, at amplitudes exceeding the activation threshold by an order of magnitude, TIS generated neuronal block, and in some cases the modulation of the total E-field caused periodic onset responses, providing an alternative mechanism for the experimental observations. Conduction block may also explain the lack of responses in off-target regions, where it can suppress endogenous brain activity. While the neuron models may overestimate absolute activation thresholds, the E-field thresholds for activation and block with TIS are, respectively, two and three orders of magnitude higher than the field strength than can be generated with tolerable levels of scalp stimulation. Therefore, administering suprathreshold TIS with transcranial electrical stimulation of the human brain appears infeasible without anesthesia and any TIS application should consider off-target effects of the carrier.

Acknowledgments

This work was supported by grants No. R01NS088674 and No. R01NS117405 from the National Institutes of Health of the United States of America; the content is solely the responsibility of the authors and does not necessarily represent the official views of the funding agency or U.S.A. government. Computational support was provided by the Duke Compute Cluster.

The authors thank Dr. Nir Grossman for providing critical feedback on preliminary results at the 2nd Carolina Neuromodulation Conference, Dr. Flavio Fröhlich for discussion on activation mechanism of TIS, Dr. Nicole A Pelot for discussion on onset response of kHz stimulation, Dr. Craig S. Henriquez and Dr. Derek M. Eidum for discussion on rotational E-fields, Dr. Sumientra Rampersad for discussion on E-field simulation in mouse model, and Dr. Huijing Xu, Dr. Gene Yu, and Dr. Alex Goddard for discussion on stimulation of hippocampal neurons.

B. W. developed the theoretical framework, designed the computational study, and performed the neural simulations and data analysis. A. S. A. developed the neuronal models and adjusted ion channel properties. W. M. G. and A.V.P. conceived, supervised, and secured funding and computational resources for the study. B. W. performed data visualization and wrote the manuscript, and all authors revised, commented on, and approved the final version of the manuscript.

Preliminary results of this study were presented at the 1st and 2nd Carolina Neuromodulation Conference (May 2018 and June 2019, Chapel Hill, NC, USA), the 43rd Neural Interface Conference (June 2018, Minneapolis, MN, USA), Neural Interfaces 2021: The NANS-NIC Joint Meeting (June 2021, online), and the 4th International Brain Stimulation Meeting [70] (December, 2021, Charleston, SC, USA).

The code and data that support the findings of this study are available online at the Research Data Repository (RDR) of Duke University Libraries: https://doi.org/10.7924/r4n87d05r.

The authors declare no competing interests.

References

[1] Eldaief M C, Press D Z and Pascual-Leone A 2013 Transcranial magnetic stimulation in neurology A review of established and prospective applications *Neurol. Clin. Pract.* **3** 519–26

[2] Lefaucheur J-P, André-Obadia N, Antal A, Ayache S S, Baeken C, Benninger D H, Cantello R M, Cincotta M, de Carvalho M, De Ridder D, Devanne H, Di Lazzaro V, Filipović S R, Hummel F C, Jääskeläinen S K, Kimiskidis V K, Koch G, Langguth B, Nyffeler T, Oliviero A, Padberg F, Poulet E, Rossi S, Rossini P M, Rothwell J C, Schönfeldt-Lecuona C, Siebner H R, Slotema C W, Stagg C J, Valls-Sole J, Ziemann U, Paulus W and Garcia-Larrea L 2014 Evidence-based guidelines on the therapeutic use of repetitive transcranial magnetic stimulation (rTMS) *Clin. Neurophysiol.* **125** 2150–206

[3] Rossi S, Antal A, Bestmann S, Bikson M, Brewer C, Brockmöller J, Carpenter L L, Cincotta M, Chen R, Daskalakis J D, Di Lazzaro V, Fox M D, George M S, Gilbert D, Kimiskidis V K, Koch G, Ilmoniemi R J, Pascal Lefaucheur J, Leocani L, Lisanby S H, Miniussi C, Padberg F, Pascual-Leone A, Paulus W, Peterchev A V, Quartarone A, Rotenberg A, Rothwell J, Rossini P M, Santarnecchi E, Shafi M M, Siebner H R, Ugawa Y, Wassermann E M, Zangen A, Ziemann U and Hallett M 2020 Safety and recommendations for TMS use in healthy subjects and patient populations, with updates on training, ethical and regulatory issues: Expert Guidelines *Clin. Neurophysiol.*

[4] Reato D, Rahman A, Bikson M and Parra L C 2013 Effects of weak transcranial alternating current stimulation on brain activity—a review of known mechanisms from animal studies *Front. Hum. Neurosci.* **7** 687

[5] Caumo W, Souza I C, Torres I L, Medeiros L, Souza A, Deitos A, Vidor L, Fregni F and Volz M S 2012 Neurobiological Effects of Transcranial Direct Current Stimulation: A Review *Front. Psychiatry* **3**

[6] Becker J E, Shultz E K B and Maley C T 2019 Transcranial Magnetic Stimulation in Conditions Other than Major Depressive Disorder *Child Adolesc. Psychiatr. Clin.* **28** 45–52

[7] Wang B, Aberra A S, Grill W M and Peterchev A V 2021 Physics and Biophysics Fundamentals of Transcranial Stimulation *The Oxford Handbook of Transcranial Stimulation* ed E M Wassermann, V Walsh, A V Peterchev, U Ziemann, S Lisanby and H Siebner (Oxford: Oxford University Press) p 23

[8] Huang Y, Liu A A, Lafon B, Friedman D, Dayan M, Wang X, Bikson M, Doyle W K, Devinsky O and Parra L C 2017 Measurements and models of electric fields in the in vivo human brain during transcranial electric stimulation *eLife* **6** e18834

[9] Miranda P C, Mekonnen A, Salvador R and Ruffini G 2013 The electric field in the cortex during transcranial current stimulation *NeuroImage* **70** 48–58

[10] Deng Z-D, Lisanby S H and Peterchev A V 2013 Electric field depth–focality tradeoff in transcranial magnetic stimulation: Simulation comparison of 50 coil designs *Brain Stimulat.* **6** 1–13

[11] Gomez L J, Goetz S M and Peterchev A V 2018 Design of transcranial magnetic stimulation coils with optimal trade-off between depth, focality, and energy *J. Neural Eng.* **15** 046033

[12] Datta A, Bansal V, Diaz J, Patel J, Reato D and Bikson M 2009 Gyri-precise head model of transcranial direct current stimulation: Improved spatial focality using a ring electrode versus conventional rectangular pad *Brain Stimulat.* **2** 201-207.e1

[13] Dmochowski J P, Datta A, Bikson M, Su Y and Parra L C 2011 Optimized multi-electrode stimulation increases focality and intensity at target *J. Neural Eng.* **8** 046011

[14] Edwards D, Cortes M, Datta A, Minhas P, Wassermann E M and Bikson M 2013 Physiological and modeling evidence for focal transcranial electrical brain stimulation in humans: A basis for high-definition tDCS *NeuroImage* **74** 266–75

[15] Huang Y and Parra L C 2019 Can transcranial electric stimulation with multiple electrodes reach deep targets? *Brain Stimulat.* **12** 30–40

[16] Grossman N, Bono D, Dedic N, Kodandaramaiah S B, Rudenko A, Suk H-J, Cassara A M, Neufeld E, Kuster N, Tsai L-H, Pascual-Leone A and Boyden E S 2017 Noninvasive Deep Brain Stimulation via Temporally Interfering Electric Fields *Cell* **169** 1029-1041.e16

[17] Vöröslakos M, Takeuchi Y, Brinyiczki K, Zombori T, Oliva A, Fernández-Ruiz A, Kozák G, Kincses Z T, Iványi B, Buzsáki G and Berényi A 2018 Direct effects of transcranial electric stimulation on brain circuits in rats and humans *Nat. Commun.* **9** 483

[18] Sorkhabi M M, Wendt K and Denison T 2020 Temporally Interfering TMS: Focal and Dynamic Stimulation Location *2020 42nd Annual International Conference of the IEEE Engineering in Medicine Biology Society (EMBC)* 2020 42nd Annual International Conference of the IEEE Engineering in Medicine Biology Society (EMBC) pp 3537–43

[19] Goats G C 1990 Interferential current therapy *Br. J. Sports Med.* **24** 87–92

[20] Kloth L 1987 Interference Current *Clinical Electrotherapy* ed R M Nelson and D P Currier (Norwalk Connecticut: Appleton & Lange) pp 183–207

[21] Kilgore K L and Bhadra N 2004 Nerve conduction block utilising high-frequency alternating current *Med. Biol. Eng. Comput.* **42** 394–406

[22] Miles J D, Kilgore K L, Bhadra N and Lahowetz E A 2007 Effects of ramped amplitude waveforms on the onset response of high-frequency mammalian nerve block *J. Neural Eng.* **4** 390

[23] Mirzakhalili E, Barra B, Capogrosso M and Lempka S F 2020 Biophysics of Temporal Interference Stimulation *Cell Syst.* **11** 557-572.e5

[24] Pelot N A, Behrend C E and Grill W M 2017 Modeling the response of small myelinated axons in a compound nerve to kilohertz frequency signals *J. Neural Eng.* **14** 046022

[25] Barker A T, Garnham C W and Freeston I L 1991 Magnetic nerve stimulation: the effect of waveform on efficiency, determination of neural membrane time constants and the measurement of stimulator output *Electroencephalogr. Clin. Neurophysiol. Suppl.* **43** 227–37

[26] D'Ostilio K, Goetz S M, Hannah R, Ciocca M, Chieffo R, Chen J-C A, Peterchev A V and Rothwell J C 2016 Effect of coil orientation on strength–duration time constant and I-wave activation with controllable pulse parameter transcranial magnetic stimulation *Clin. Neurophysiol.* **127** 675–83

[27] Peterchev A V, Goetz S M, Westin G G, Luber B and Lisanby S H 2013 Pulse width dependence of motor threshold and input–output curve characterized with controllable pulse parameter transcranial magnetic stimulation *Clin. Neurophysiol.* **124** 1364–72

[28] Dmochowski J and Bikson M 2017 Noninvasive Neuromodulation Goes Deep *Cell* **169** 977–8

[29] Gomez-Tames J, Asai A and Hirata A 2021 Multiscale Computational Model Reveals Nerve Response in a Mouse Model for Temporal Interference Brain Stimulation *Front. Neurosci.* **15**

[30] Howell B and McIntyre C C 2020 Feasibility of Interferential and Pulsed Transcranial Electrical Stimulation for Neuromodulation at the Human Scale *Neuromodulation Technol. Neural Interface* **n/a**

[31] Aberra A S, Wang B, Grill W M and Peterchev A V 2020 Simulation of transcranial magnetic stimulation in head model with morphologically-realistic cortical neurons *Brain Stimulat.* **13** 175–89

[32] Esmaeilpour Z, Kronberg G, Reato D, Parra L C and Bikson M 2021 Temporal interference stimulation targets deep brain regions by modulating neural oscillations *Brain Stimulat.* **14** 55–65

[33] Lee S, Lee C, Park J and Im C-H 2020 Individually customized transcranial temporal interference stimulation for focused modulation of deep brain structures: a simulation study with different head models *Sci. Rep.* **10** 11730

[34] Lee S, Park J, Choi D S, Lee C and Im C-H 2022 Multipair transcranial temporal interference stimulation for improved focalized stimulation of deep brain regions: A simulation study *Comput. Biol. Med.* **143** 105337

[35] Rampersad S, Roig-Solvas B, Yarossi M, Kulkarni P P, Santarnecchi E, Dorval A D and Brooks D H 2019 Prospects for transcranial temporal interference stimulation in humans: A computational study *NeuroImage* **202** 116124

[36] Song X, Zhao X, Li X, Liu S and Ming D 2021 Multi-channel transcranial temporally interfering stimulation (tTIS): application to living mice brain *J. Neural Eng.* **18** 036003

[37] Alekseichuk I, Mantell K, Shirinpour S and Opitz A 2019 Comparative modeling of transcranial magnetic and electric stimulation in mouse, monkey, and human *NeuroImage* **194** 136–48

[38] Louviot S, Tyvaert L, Maillard L G, Colnat-Coulbois S, Dmochowski J and Koessler L 2022 Transcranial Electrical Stimulation generates electric fields in deep human brain structures *Brain Stimulat.* **15** 1–12

[39] Plonsey R and Heppner D B 1967 Considerations of quasi-stationarity in electrophysiological systems *Bull. Math. Biophys.* **29** 657–64

[40] Bossetti C A, Birdno M J and Grill W M 2008 Analysis of the quasi-static approximation for calculating potentials generated by neural stimulation *J. Neural Eng.* **5** 44–53

[41] Bikson M, Dmochowski J and Rahman A 2013 The "Quasi-Uniform" Assumption in Animal and Computational Models of Non-Invasive Electrical Stimulation *Brain Stimulat.* **6** 704–5

[42] Aberra A S, Peterchev A V and Grill W M 2018 Biophysically Realistic Neuron Models for Simulation of Cortical Stimulation *J. Neural Eng.* **15** 066023

[43] Alekseichuk I, Falchier A Y, Linn G, Xu T, Milham M P, Schroeder C E and Opitz A 2019 Electric field dynamics in the brain during multi-electrode transcranial electric stimulation *Nat. Commun.* **10** 2573

[44] Rotem A, Neef A, Neef N E, Agudelo-Toro A, Rakhmilevitch D, Paulus W and Moses E 2014 Solving the Orientation Specific Constraints in Transcranial Magnetic Stimulation by Rotating Fields *PLOS ONE* **9** e86794

[45] Roth Y, Pell G, Ankry M, Hadad Y, Eisen A, Burnishev Y, Tendler A, Moses E and Zangen A 2019 Comparing rotational-field-dTMS to unidirectional-dTMS in healthy volunteers *Brain Stimulat.* **12** 390

[46] Roth Y, Pell G S, Barnea-Ygael N, Ankry M, Hadad Y, Eisen A, Burnishev Y, Tendler A, Moses E and Zangen A 2020 Rotational field TMS: Comparison with conventional TMS based on motor evoked potentials and thresholds in the hand and leg motor cortices *Brain Stimulat.* **13** 900–7

[47] Markram H, Muller E, Ramaswamy S, Reimann M W, Abdellah M, Sanchez C A, Ailamaki A, Alonso-Nanclares L, Antille N, Arsever S, Kahou G A A, Berger T K, Bilgili A, Buncic N, Chalimourda A, Chindemi G, Courcol J-D, Delalondre F, Delattre V, Druckmann S, Dumusc R, Dynes J, Eilemann S, Gal E, Gevaert M E, Ghobril J-P, Gidon A, Graham J W, Gupta A, Haenel V, Hay E, Heinis T, Hernando J B, Hines M, Kanari L, Keller D, Kenyon J, Khazen G, Kim Y, King J G, Kisvarday Z, Kumbhar P, Lasserre S, Le Bé J-V, Magalhães B R C, Merchán-Pérez A, Meystre J, Morrice B R, Muller J, Muñoz-Céspedes A, Muralidhar S, Muthurasa K, Nachbaur D, Newton T H, Nolte M, Ovcharenko A, Palacios J, Pastor L, Perin R, Ranjan R, Riachi I, Rodríguez J-R, Riquelme J L, Rössert C, Sfyrakis K, Shi Y, Shillcock J C, Silberberg G, Silva R, Tauheed F, Telefont M, Toledo-Rodriguez M, Tränkler T, Van Geit W, Díaz J V, Walker R, Wang Y, Zaninetta S M, DeFelipe J, Hill S L, Segev I and Schürmann F 2015 Reconstruction and Simulation of Neocortical Microcircuitry *Cell* **163** 456–92

[48] Ramaswamy S, Courcol J-D, Abdellah M, Adaszewski S R, Antille N, Arsever S, Atenekeng G, Bilgili A, Brukau Y, Chalimourda A, Chindemi G, Delalondre F, Dumusc R, Eilemann S, Gevaert M E, Gleeson P, Graham J W, Hernando J B, Kanari L, Katkov Y, Keller D, King J G, Ranjan R, Reimann M W, Rössert C, Shi Y, Shillcock J C, Telefont M, Van Geit W, Villafranca Diaz J, Walker R, Wang Y, Zaninetta S M, DeFelipe J, Hill S L, Muller J, Segev I, Schürmann F, Muller E B and Markram H 2015 The neocortical microcircuit collaboration portal: a resource for rat somatosensory cortex *Front. Neural Circuits* **9**

[49] Hines M L and Carnevale N T 1997 The NEURON Simulation Environment *Neural Comput.* **9** 1179–209

[50] Engel D and Jonas P 2005 Presynaptic Action Potential Amplification by Voltage-Gated Na+ Channels in Hippocampal Mossy Fiber Boutons *Neuron* **45** 405–17

[51] Schmidt-Hieber C and Bischofberger J 2010 Fast Sodium Channel Gating Supports Localized and Efficient Axonal Action Potential Initiation *J. Neurosci.* **30** 10233–42

[52] Wang B, Aberra A S, Grill W M and Peterchev A V 2018 Modified cable equation incorporating transverse polarization of neuronal membranes for accurate coupling of electric fields *J. Neural Eng.* **15** 026003

[53] Fröhlich F and McCormick D A 2010 Endogenous Electric Fields May Guide Neocortical Network Activity *Neuron* **67** 129–43

[54] Reato D, Rahman A, Bikson M and Parra L C 2010 Low-Intensity Electrical Stimulation Affects Network Dynamics by Modulating Population Rate and Spike Timing *J. Neurosci.* **30** 15067–79

[55] Krause M R, Vieira P G, Csorba B A, Pilly P K and Pack C C 2019 Transcranial alternating current stimulation entrains single-neuron activity in the primate brain *Proc. Natl. Acad. Sci.* 201815958

[56] Deng Z-D, Lisanby S H and Peterchev A V 2011 Electric field strength and focality in electroconvulsive therapy and magnetic seizure therapy: a finite element simulation study *J. Neural Eng.* **8** 016007

[57] Lee W H, Lisanby S H, Laine A F and Peterchev A V 2015 Electric Field Model of Transcranial Electric Stimulation in Nonhuman Primates: Correspondence to Individual Motor Threshold *IEEE Trans. Biomed. Eng.* **62** 2095–105

[58] Regenold W T, Noorani R J, Piez D and Patel P 2015 Nonconvulsive electrotherapy for treatment resistant unipolar and bipolar major depressive disorder: a proof-of-concept trial *Brain Stimulat.* **8** 855–861

[59] Huang Y, Datta A and Parra L C 2020 Optimization of interferential stimulation of the human brain with electrode arrays *J. Neural Eng.* **17** 036023

[60] de Cheveigné A and Nelken I 2019 Filters: When, Why, and How (Not) to Use Them *Neuron* **102** 280–93

[61] Aberra A S, Lopez A, Grill W M and Peterchev A V 2022 Rapid estimation of cortical neuron activation thresholds by transcranial magnetic stimulation using convolutional neural networks *bioRxiv* 2022.05.18.490331

[62] Colbert C M and Pan E 2002 Ion channel properties underlying axonal action potential initiation in pyramidal neurons *Nat. Neurosci.* **5** 533

[63] Cao J and Grover P 2019 STIMULUS: Noninvasive Dynamic Patterns of Neurostimulation Using Spatio-Temporal Interference *IEEE Trans. Biomed. Eng.*

[64] Xiao Q, Zhong Z, Lai X and Qin H 2019 A multiple modulation synthesis method with high spatial resolution for noninvasive neurostimulation *PLOS ONE* **14** e0218293

[65] McIntyre C C, Richardson A G and Grill W M 2002 Modeling the Excitability of Mammalian Nerve Fibers: Influence of Afterpotentials on the Recovery Cycle *J. Neurophysiol.* **87** 995–1006

[66] Luber B, Davis S W, Deng Z-D, Murphy D, Martella A, Peterchev A V and Lisanby S H 2022 Using diffusion tensor imaging to effectively target TMS to deep brain structures *NeuroImage* **249** 118863

[67] Ulrich M, Lorenz S, Spitzer M W, Steigleder L, Kammer T and Grön G 2018 Theta-burst modulation of mid-ventrolateral prefrontal cortex affects salience coding in the human ventral tegmental area *Appetite* **123** 91–100

[68] Wang J X, Rogers L M, Gross E Z, Ryals A J, Dokucu M E, Brandstatt K L, Hermiller M S and Voss J L 2014 Targeted enhancement of cortical-hippocampal brain networks and associative memory *Science* **345** 1054–7

[69] Weigand A, Horn A, Caballero R, Cooke D, Stern A P, Taylor S F, Press D, Pascual-Leone A and Fox M D 2018 Prospective Validation That Subgenual Connectivity Predicts Antidepressant Efficacy of Transcranial Magnetic Stimulation Sites *Biol. Psychiatry* **84** 28–37

[70] Wang B, Aberra A, Grill W and Peterchev A 2021 Comparing temporal interference stimulation and other kilohertz stimulation modalities using computational models *Brain Stimulat.* **14** 1679

Supplement

Responses of Model Cortical Neurons to Temporal Interference Stimulation and Related Transcranial Alternating Current Stimulation Modalities

Boshuo Wang[1], Aman S. Aberra[2,#], Warren M. Grill[2,3,4,5], Angel V. Peterchev[1,2,3,5,*]

[1] Department of Psychiatry and Behavioral Sciences, School of Medicine, Duke University, Durham, NC 27710, USA

[2] Department of Biomedical Engineering, School of Engineering, Duke University, Durham, NC 27708, USA

[3] Department of Electrical and Computer Engineering, School of Engineering, Duke University, Durham, NC 27708, USA

[4] Department of Neurobiology, School of Medicine, Duke University, Durham, NC 27710, USA

[5] Department of Neurosurgery, School of Medicine, Duke University, Durham, NC 27710, USA

[*] Corresponding author: angel.peterchev@duke.edu

[#] A. S. Aberra is currently with the Department of Biological Sciences, Dartmouth College, Hanover, NH 03755, USA.

Contents:

Figures S1–S14

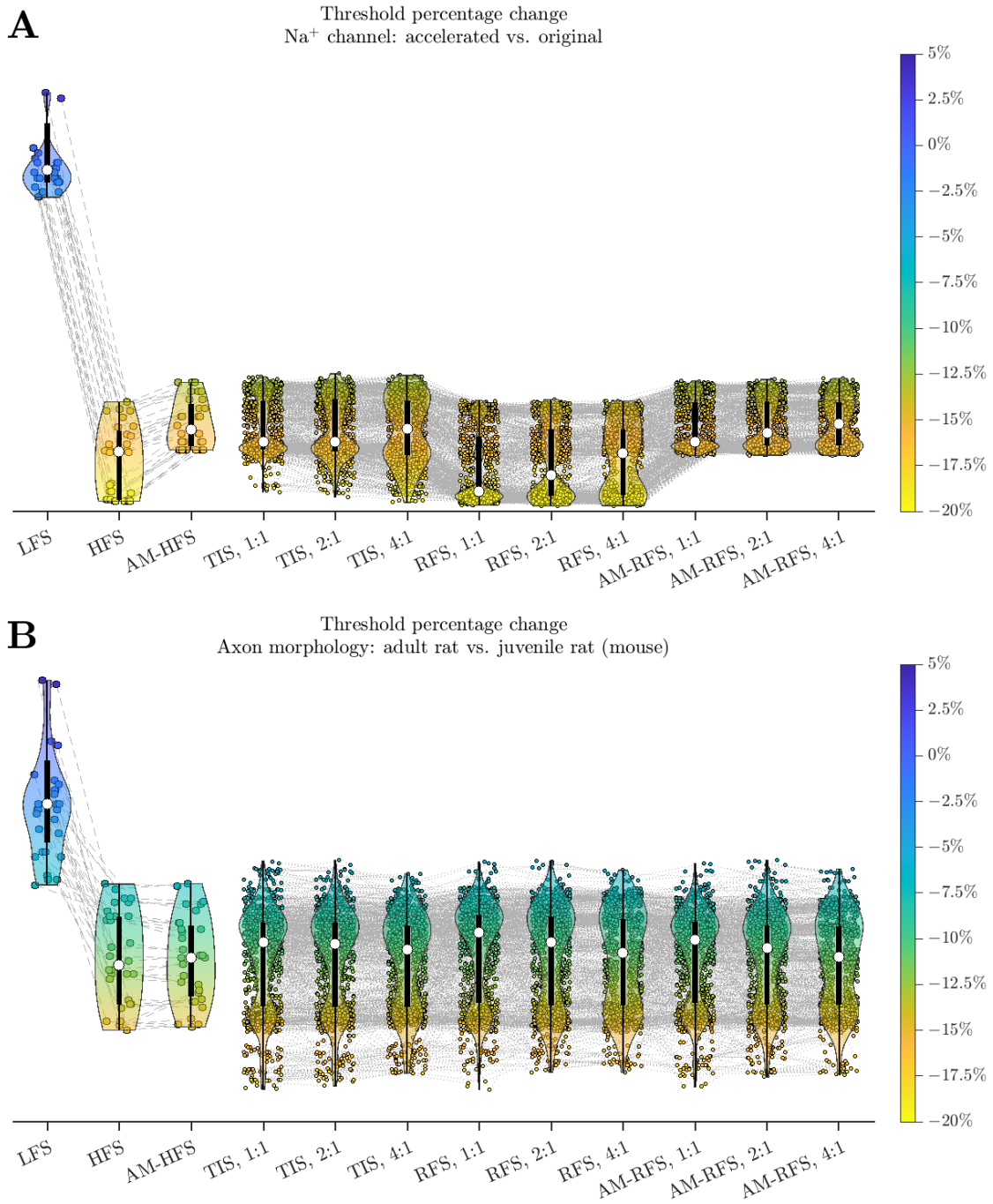

Figure S1. Changes of activation thresholds for modification applied to the neuron models

A. Percentage changes of thresholds of the tACS modalities across E-field orientations comparing accelerated sodium channel dynamics versus original. **B.** Percentage changes of thresholds of the tACS modalities across E-field orientations for neuron models scaled to size of adult rat from original size of juvenile rat. The latter size is used to simulate adult mice in this study. The limited change of thresholds demonstrate that the size difference between rat and mouse neurons is not critical for comparing the neuronal response to the types of stimulation in this study. Figure format is overall similar to Figure 6. Outliers of LFS were excluded. The gray dashed lines connect the same E-field orientations between the quasistatic modalities and orientation combinations between the non-quasistatic modalities.

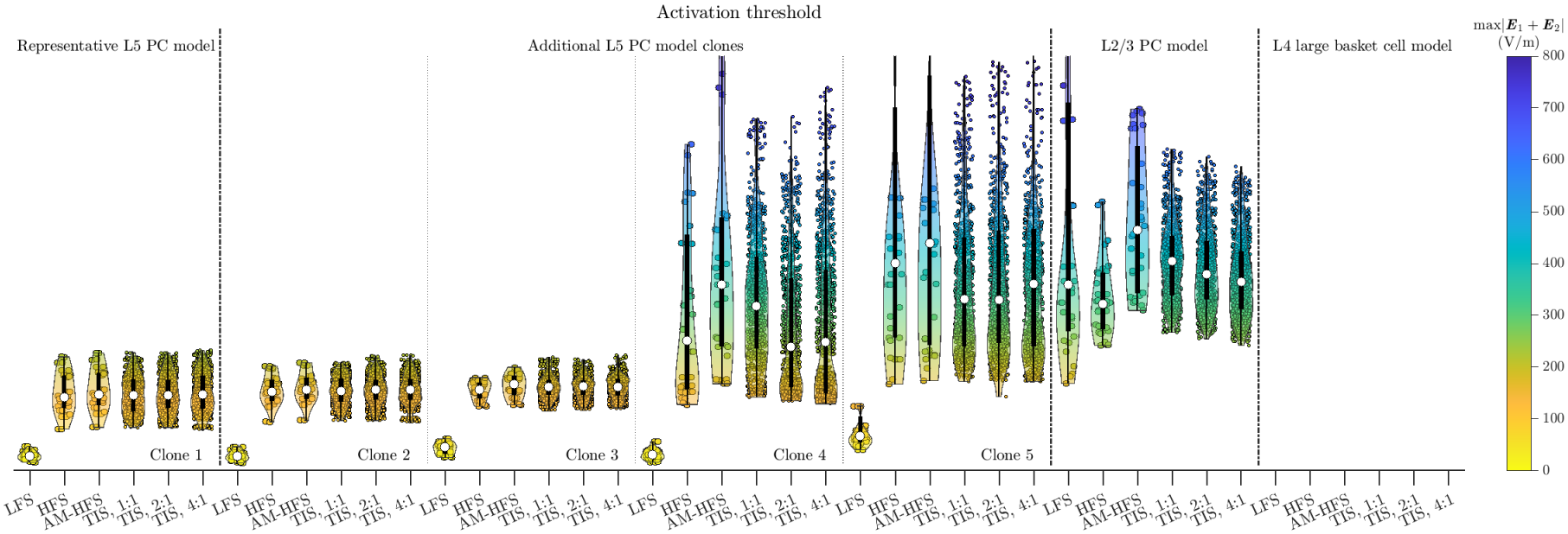

Figure S2. Activation thresholds of LFS, HFS, AM-HFS, and TIS for five model clones of the layer 5 pyramidal cell (L5 PC), one layer 2/3 PC, and one layer 4 interneuron

Figure format is overall similar to Figure 6, with the results for each clone separated by vertical dashed lines. The representative L5 model (clone No. 1) used is shown on the left. Two L5 clones (No. 2 and 3) have threshold distributions similar to the representative model, whereas the other two clones have wider threshold distributions for kHz tACS due to their axon morphologies. For the latter two L5 clones (No. 4 and 5), the ratio of the lowest kHz thresholds versus LFS thresholds is comparable to those of the first three clones. Moreover, the additional clones do not exhibit lower absolute thresholds than the representative model. Therefore, the conclusions in the main text based on the representative L5 model hold generally. The L2/3 PC also has higher threshold for all stimulation modalities than the representative L5 model, and the LFS threshold had a wide range due to the model neuron lacking axon terminals aligned with some orientations of the E-field. Due to its dense dendritic morphology and different ion channel conductivities, the L4 interneuron had thresholds $\gg$ 1 kV/m for a few E-field orientations whereas for the majority of E-field orientations it could not be activated periodically at 10 Hz by E-field of strength in the search range up to 4000 V/m. Therefore the results of L4 interneuron are not visible in the figure.

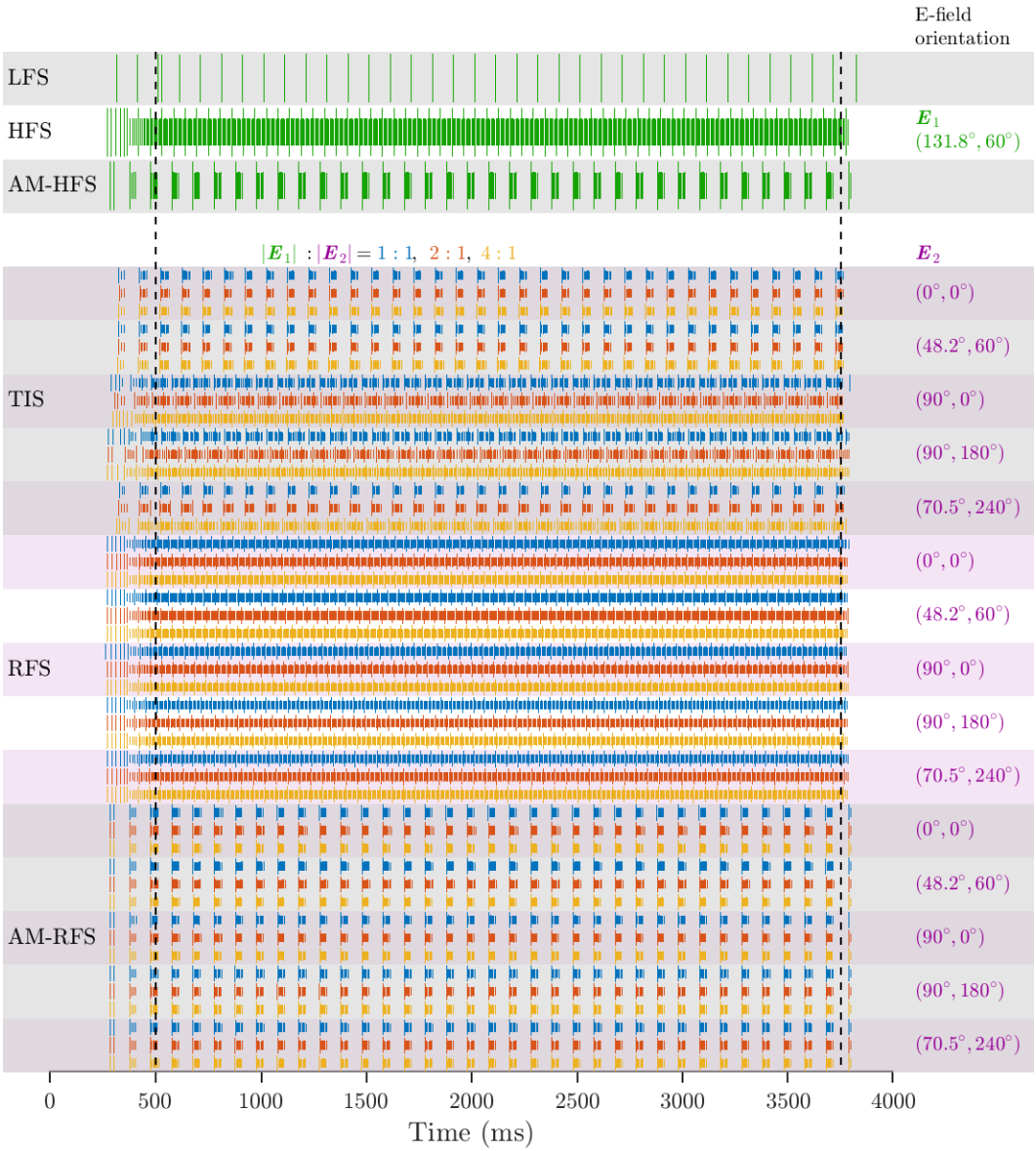

Figure S3. Representative suprathreshold responses of L5 PC

Raster plot of somatic firing for stimulation amplitude at 1.5 times activation threshold as shown in Figure 5. The first spike within each burst is shown with a longer line.

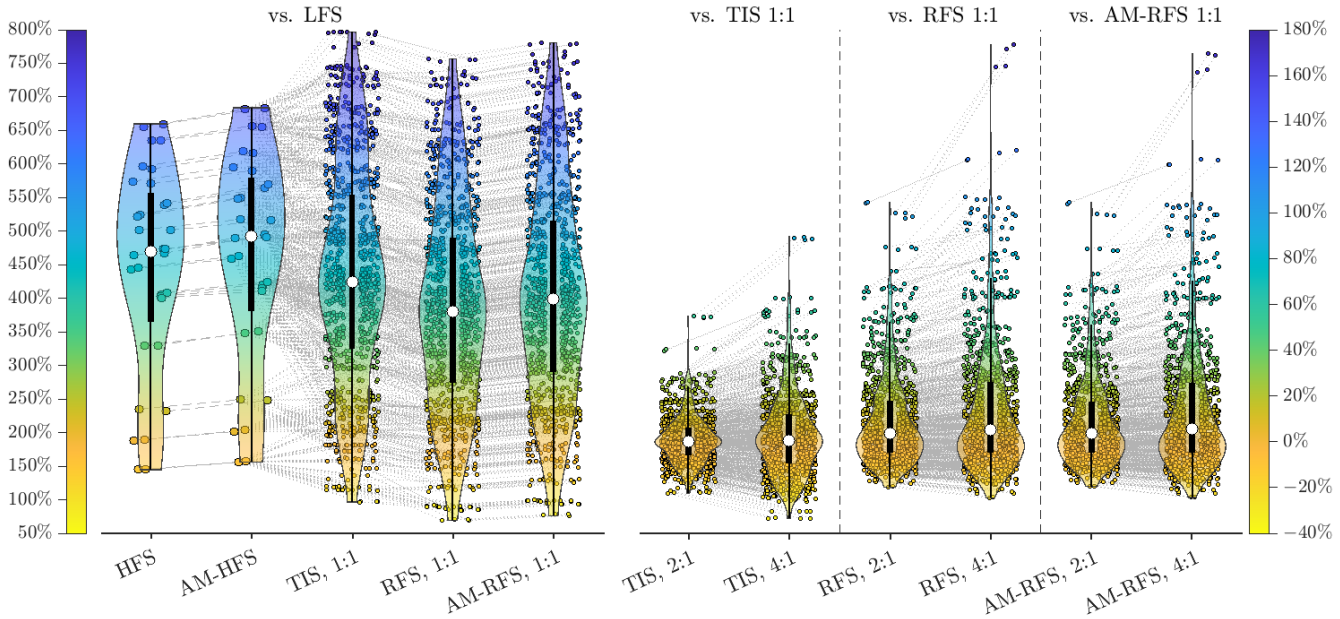

Figure S4. Changes of activation thresholds

Left: percentage changes of thresholds versus LFS for HFS and AM-HFS, as well as TIS, RFS, and AM-RFS of equal E-field amplitudes. For HFS and AM-HFS, the changes were calculated against LFS with the same E-field orientation. For TIS, RFS, and AM-RFS, the comparison was against LFS with the E-field orientation aligning closest with the E-field orientation at maximum amplitude. The gray dashed lines connect the same E-field orientations between HFS and AM-HFS and orientation combinations between the non-quasistatic modalities, and links the E-field orientation of the quasistatic stimulation modalities with the closest non-quasistatic E-field at maximum amplitude. Right: percentage changes of thresholds of non-quasistatic tACS modalities with unequal E-field versus equal E-field. Figure format is similar to Figure 6.

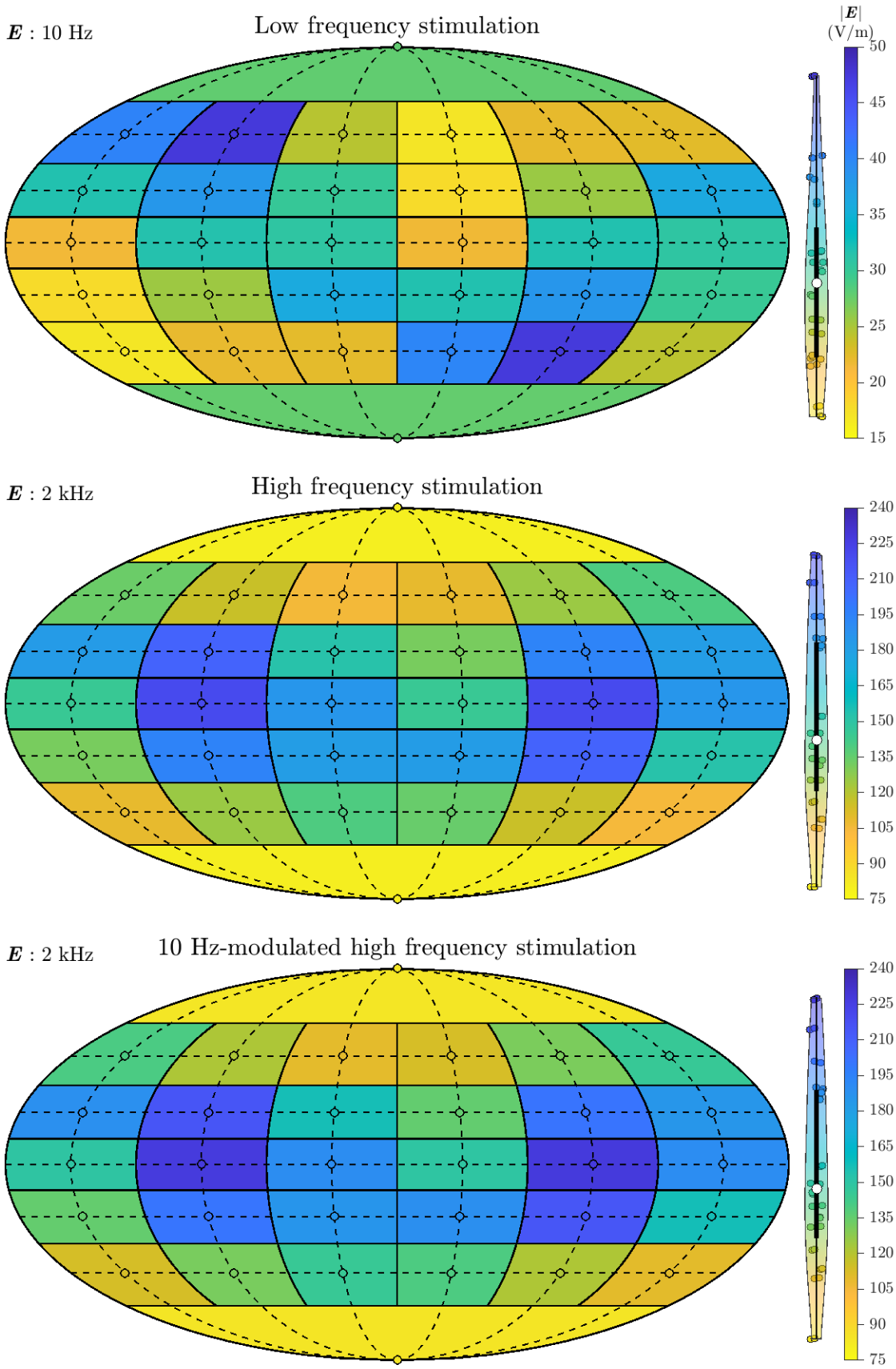

Figure S5. Distributions of activation threshold for all E-field orientations of LFS, HFS, AM-HFS

The orientations of the E-field is converted from its spherical arguments into 2D coordinates with Mollweide projection. Each patch shows the threshold of one orientation (circle) with dashed line showing the grid of the E-field sampling in the spherical coordinate. Violin plots are similar to those in Figure 6 with different ranges.

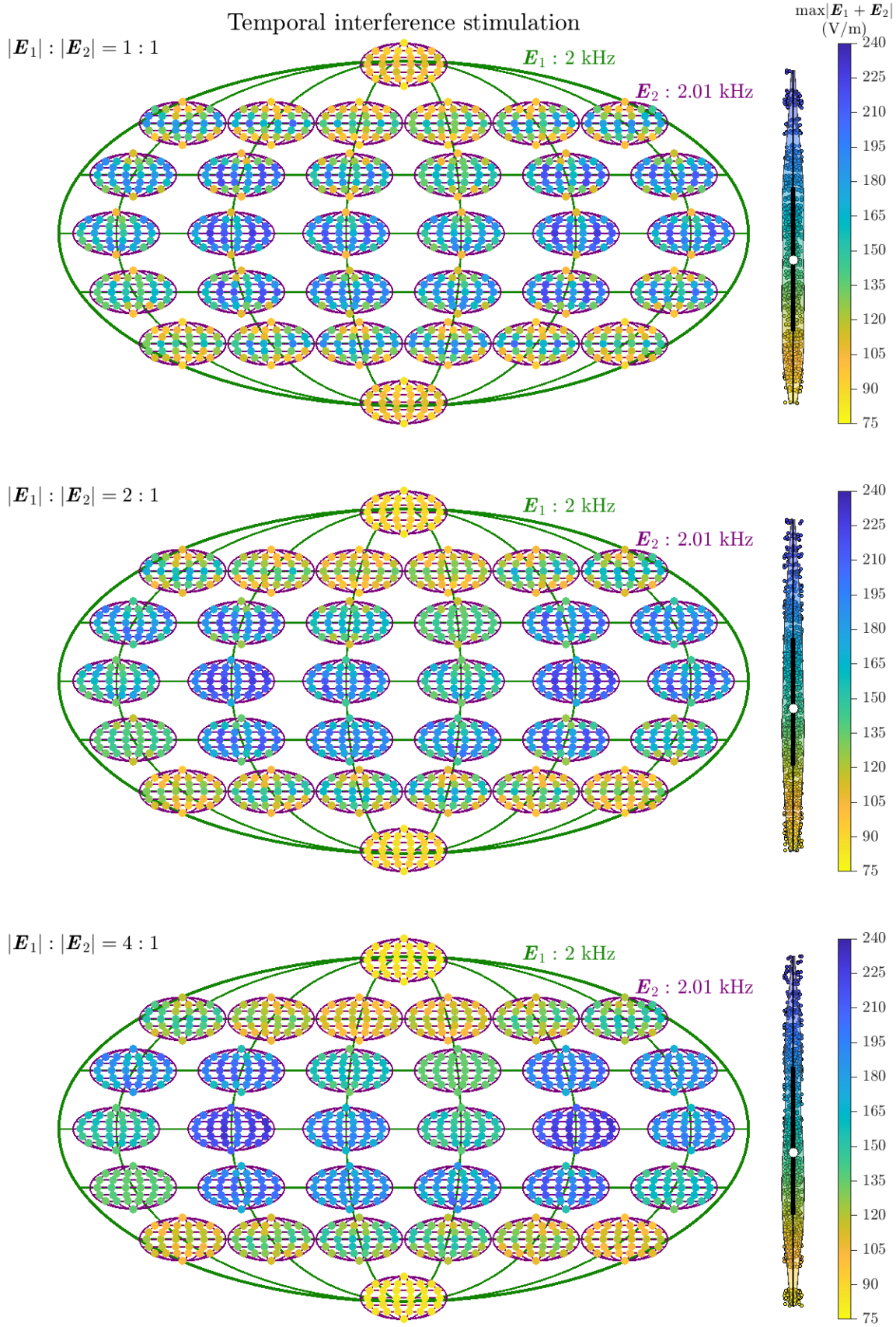

Figure S6. Distributions of activation threshold for all E-field orientation combinations of TIS

Both E-fields $\boldsymbol{E}_{1,2}$ are mapped using Mollweide projection, with the smaller maps showing the thresholds for all 32 orientations of the second E-field $\boldsymbol{E}_2$ for a fixed orientation of the first E-field $\boldsymbol{E}_1$, and the smaller maps are arranged according to the orientations of $\boldsymbol{E}_1$. Violin plots are similar to those in Figure 6 with different ranges.

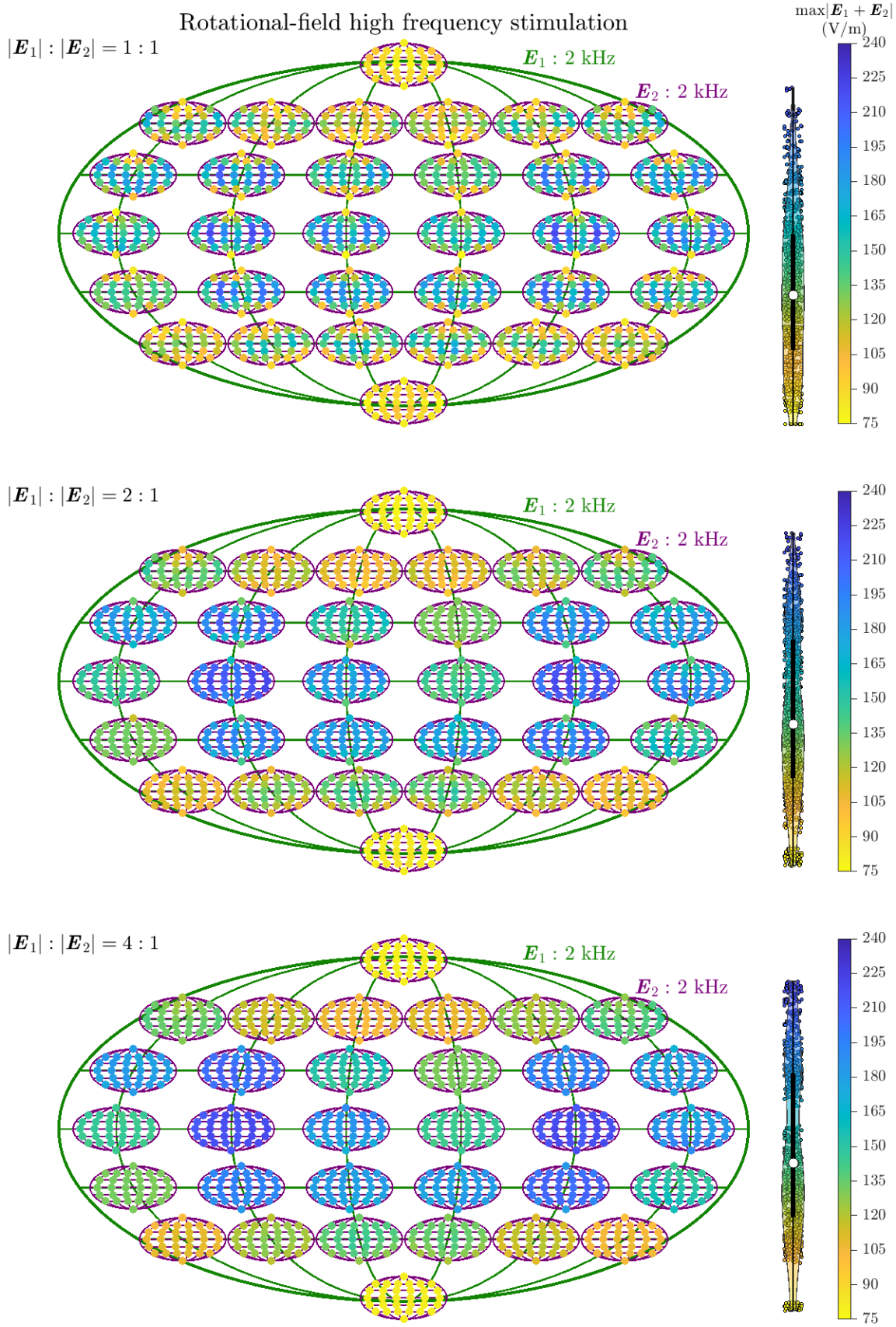

Figure S7. Distributions of activation threshold for all E-field orientation combinations of RFS
Same format as Figure S6.

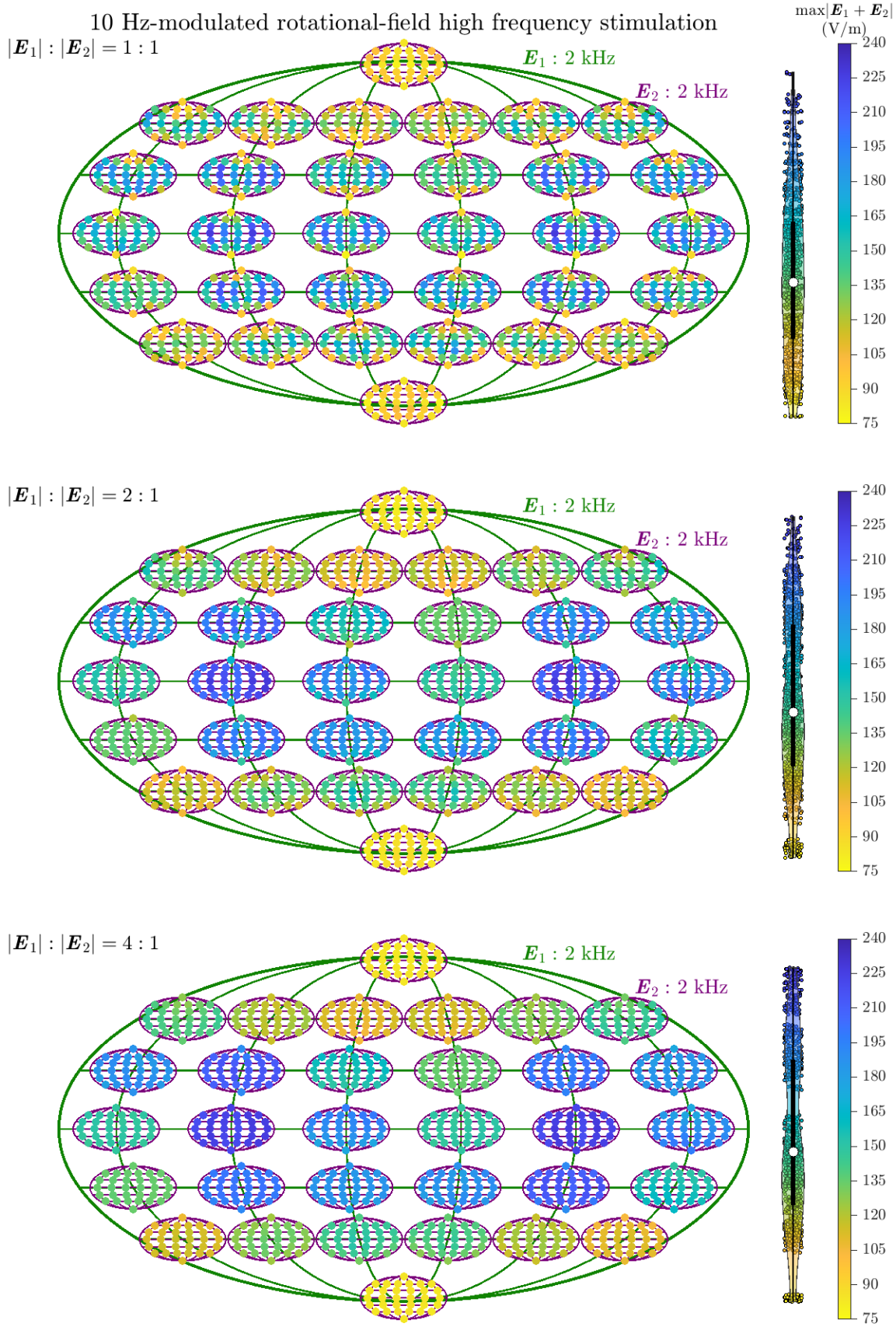

Figure S8. Distributions of activation threshold for all E-field orientation combinations of AM-RFS
Same format as Figure S6.

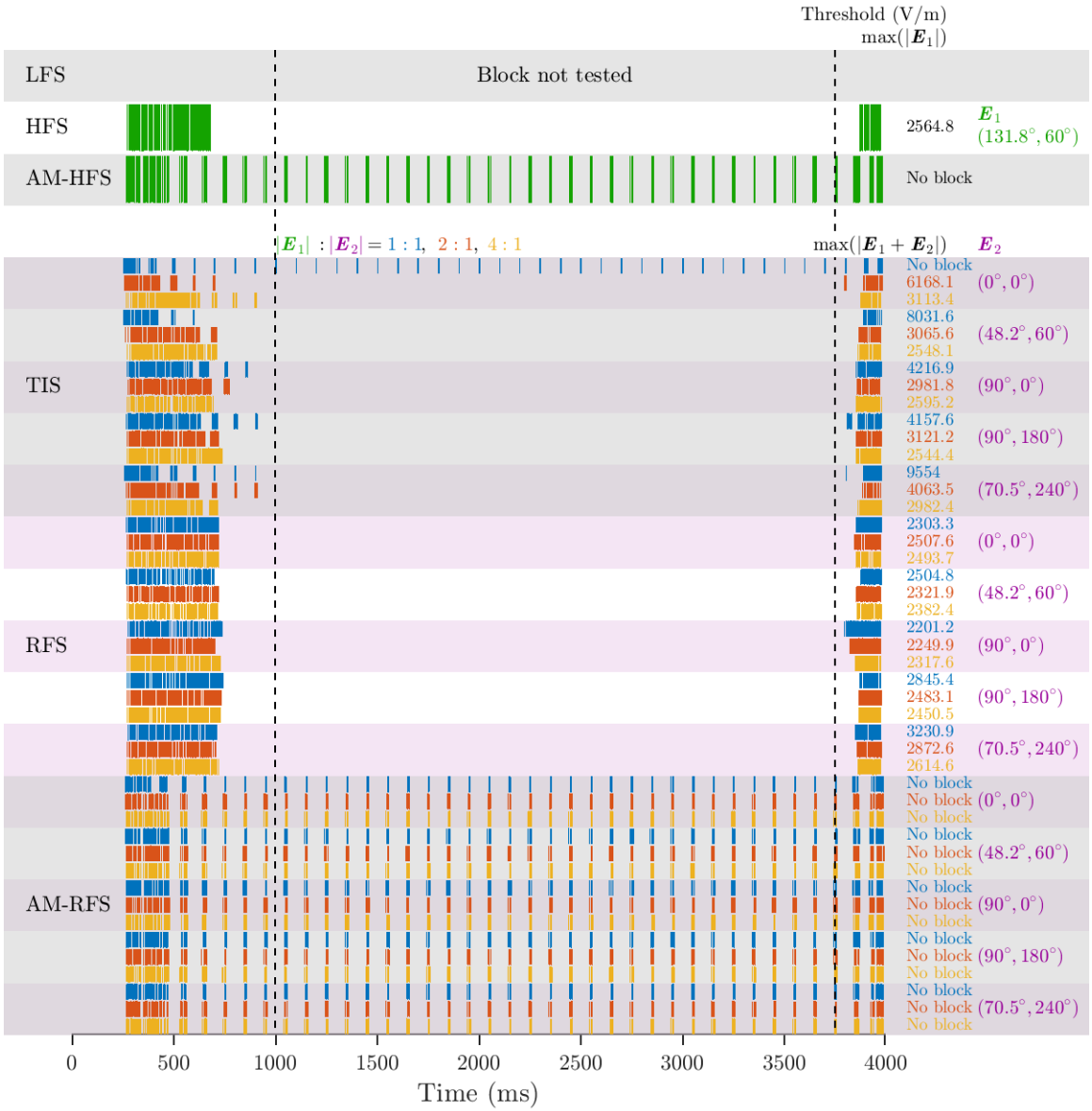

Figure S9. Representative responses of L5 PC at conduction block thresholds or maximum amplitude tested
Same as Figure 7, but for spikes of the raw transmembrane potential.

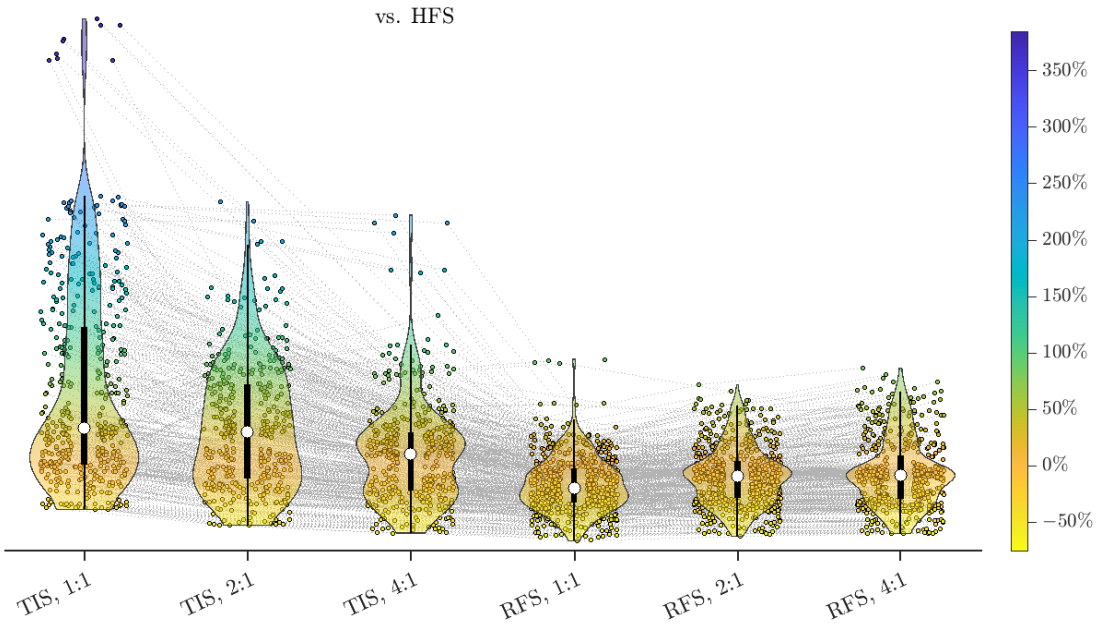

Figure S10. Changes of conduction block thresholds

Percentage changes of TIS and RFS thresholds versus HFS, calculate against HFS with E-field orientation aligning closest with the TIS or RFS E-field orientation at maximum amplitude. The gray dashed lines connect the same E-field orientation combinations between the non-quasistatic modalities. Similar format as Figure S4.

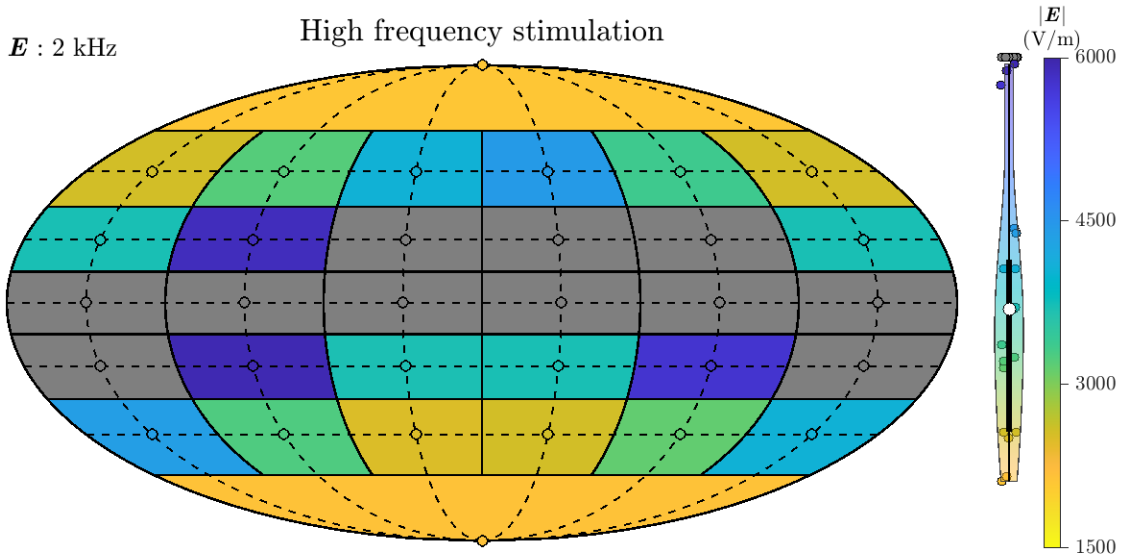

Figure S11. Distributions of conduction block threshold for all E-field orientations of HFS

Similar format as Figure S5. Grey data points indicate that conduction block could not be achieved within 6000 V/m.

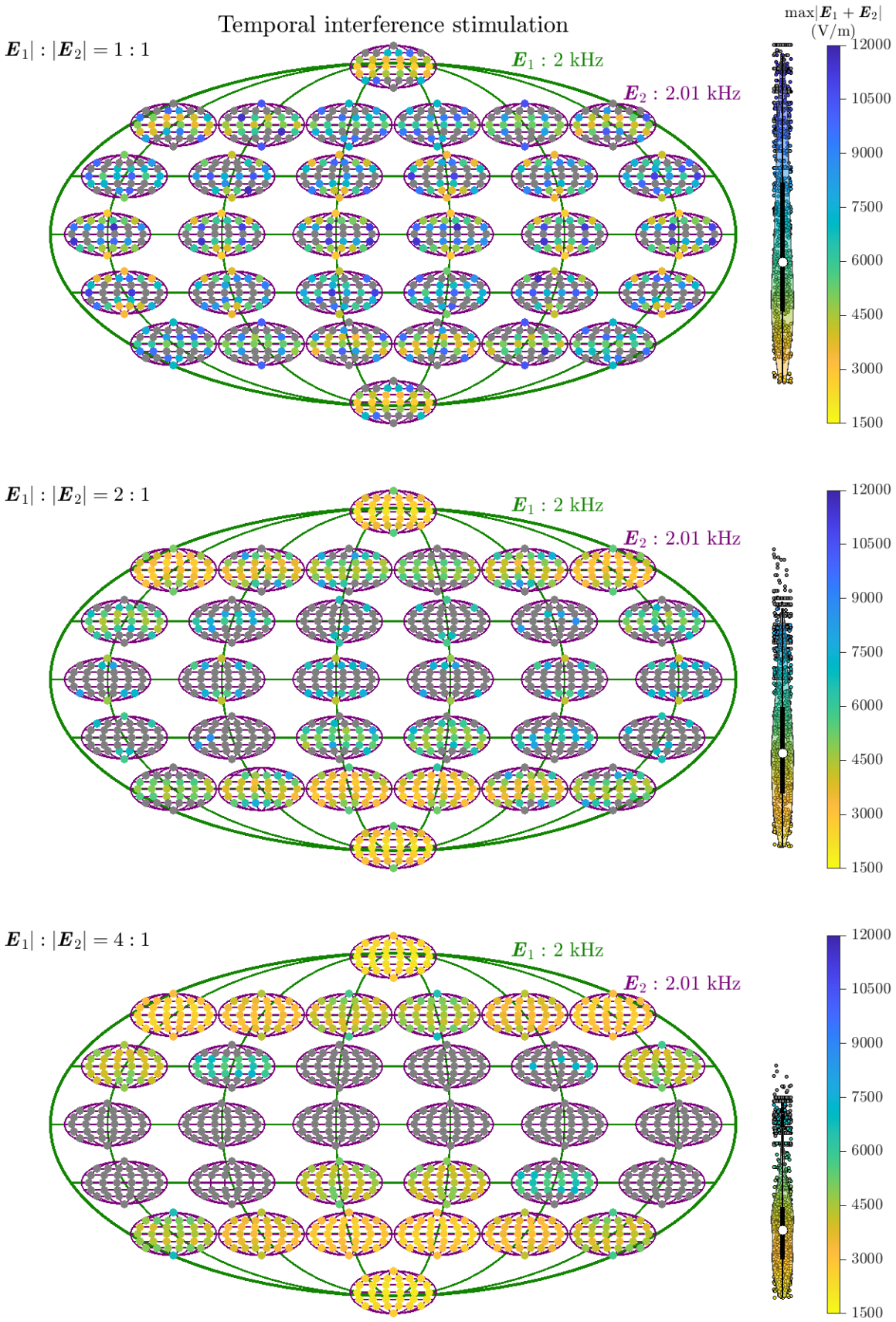

Figure S12. Distributions of conduction block threshold for all E-field orientation combinations of TIS
Similar format as Figure S6. Gray data points indicate that block could not be achieved within 6000 V/m.

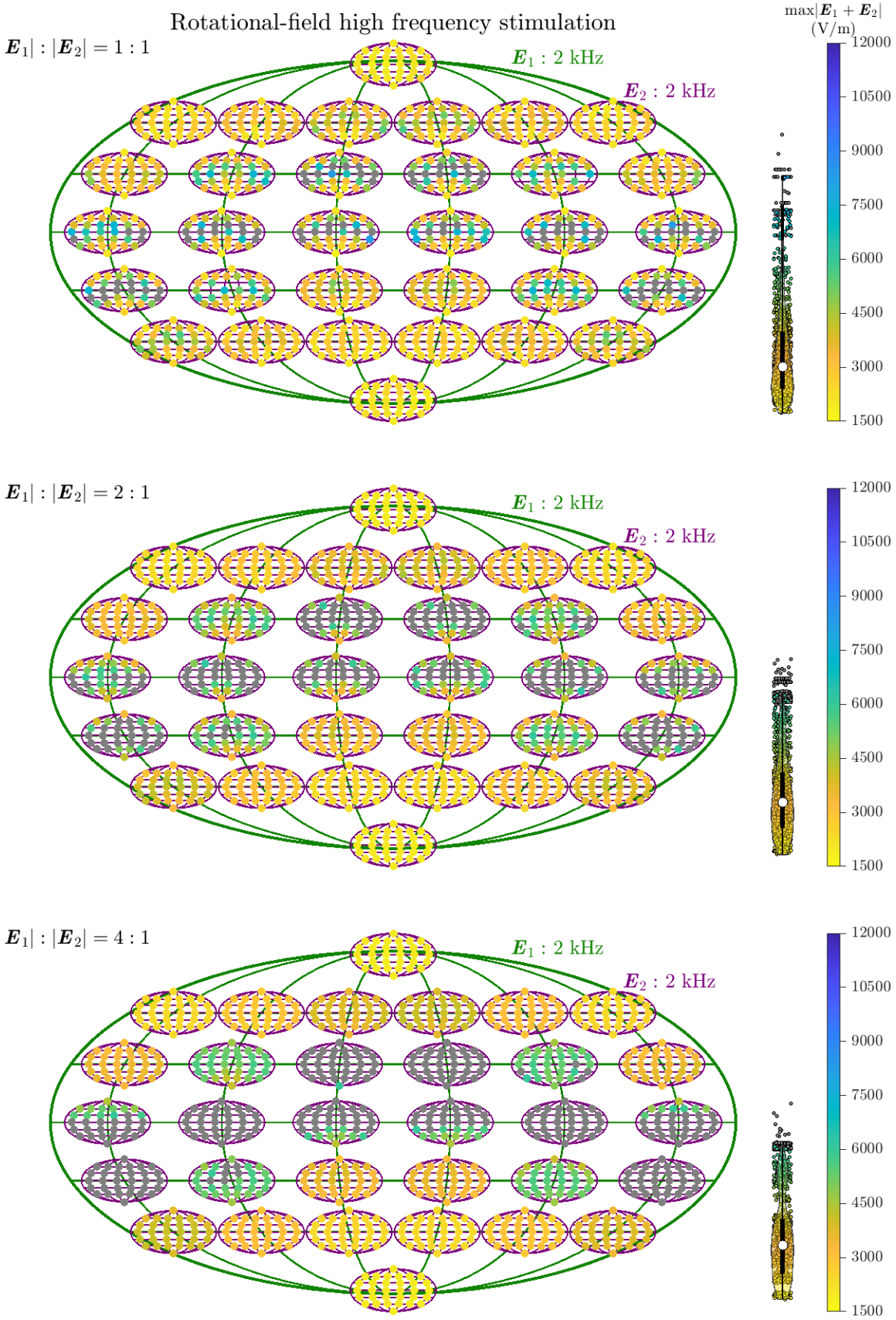

Figure S13. Distributions of conduction block threshold for all E-field orientation combinations of RFS
Same format as Figure S12.

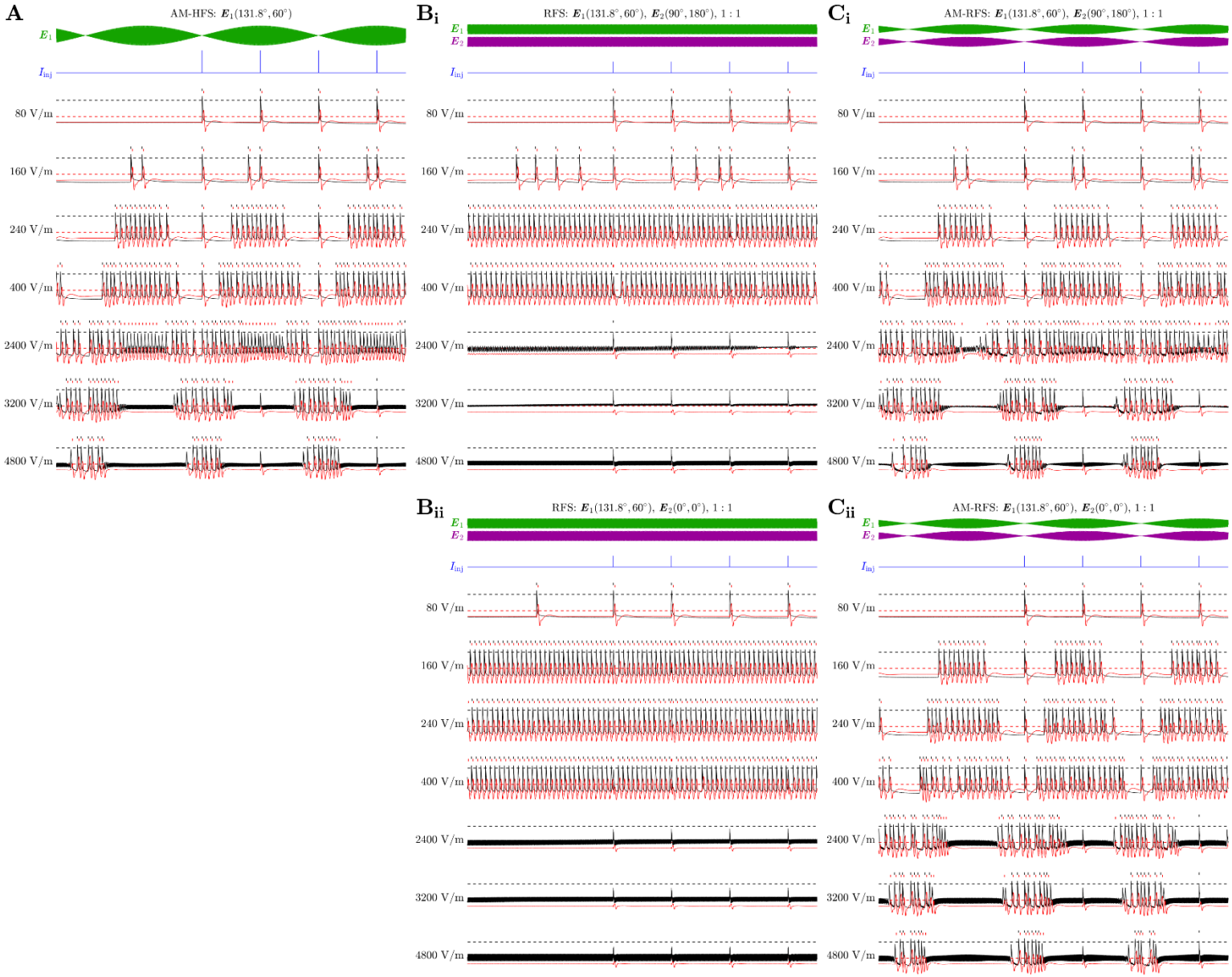

Figure S14. Neuron firing evoked by AM-HFS, RFS and AM-RFS for a range of representative E-field amplitudes

Similar format as Figure 8. E-field amplitudes are given as either max($|\boldsymbol{E}_1|$) for AM-HFS or max($|\boldsymbol{E}_1+\boldsymbol{E}_2|$) for RFS and AM-RFS. **A.** AM-HFS evokes periodic firing, which shifts from the maximum of the envelope to the minimum for high stimulation amplitude, indicating that the firing becomes an onset/offset response. Test pulses injected at the maximum of the envelope are blocked. **B.** RFS results in sustained firing that is blocked at higher stimulation amplitudes. **C.** AM-RFS results in periodic activation that shifts from the maximum of the envelope to the minimum like AM-HFS. The test pulses at the maximum of the envelope are blocked.